Correlated Two-Photon Metrology

M.P Vaughan

A project conducted at the

National Physical Laboratory
Queens Road, Teddington
TW11 0LW, UK

and submitted as a dissertation for the

MSc in the Physics of Laser Communications

Dept. of Electronic Systems Engineering
University of Essex

2003

Abstract

Research has been ongoing in the field of quantum metrology using correlated photons to establish radiometric scales in the photon counting regime without the need of calibrated detectors or sources. Currently, detector and source scales are traced ultimately to the SI unit of electricity. The use of correlated photons offers methods for establishing these scales absolutely. This removes the need for long calibration chains for the determination of detector quantum efficiency (QE) and enables radiation scales to be based on fundamental constants. A further advantage in the determination of spectral radiance is the possibility of using detectors in the visible range to measure sources in the IR. The focus of current work is to establish and improve the levels of uncertainty associated with these methods in order that they become viable techniques.

Table of Contents

1. Introduction

In recent years there has been growing interest in the area of quantum metrology. This new field has its theoretical roots in the physics of *entangled* or *correlated* states. Entities, e.g. photons, may be produced in pairs (or groups of higher number) and their dynamic properties then remain correlated, in accordance with the conservation laws of energy and momentum. Measuring, say, the momentum of one particle means knowing instantly the momentum of the other, even when they are separated over space.

This has historically been a point of contention for some physicists, notably Einstein who argued that quantum mechanics must be an incomplete description of nature as such action-at-a-distance would contradict Special Relativity. According to quantum mechanics, knowledge of such dynamical variables is usually limited by the Heisenburg Uncertainty Principle. Thus, measuring the state of one entity means instantaneously determining the state of its separated but correlated partner, which would seem to imply a faster than light signal. In fact, since no actual information is communicated over spacetime in this way, Relativity theory remains intact and the phenomenon of entanglement has been verified experimentally [i].

Quantum metrology seeks to exploit the use of correlated photons to develop measurement techniques in the photon counting regime that do not rely on existing calibrated standards and which can be tied to fundamental constants. Current radiation scales are based on cryogenic radiometry [ii]. This is a technique based on electrical substitution radiometry (ESR) in which the heating effect of an optical source is compared to electrical heating. Thus the primary scales are based on the SI unit of the

Ampere. Cryogenic radiometers are then used to calibrate trap detectors, which in turn are used to calibrate filter radiometers. The latter are used to measure spectral radiance. By cooling to temperatures below 20 K, cryogenic radiometry has enabled the realisation of detector scales with uncertainties of 0.005%. The uncertainties in the scales for radiant sources are currently 0.5%.

The quantum methods use correlated pairs of photons produced by parametric downconversion (PDC) in a nonlinear crystal. In this process, an incident pump photon decays into two daughter photons, conventionally called the *signal* and the *idler*, with energy and conservation being conserved. This can be expressed as

$$\begin{aligned} \omega_p &= \omega_s + \omega_i \\ \mathbf{k}_p &= \mathbf{k}_s + \mathbf{k}_i \end{aligned} \tag{1.1}$$

where the ω_i are the angular frequencies and the $\mathbf{k}_i$ are the wavevectors of the pump and daughter photons. These equations are known as the *phase-matching* conditions as they also arise out of a classical analysis of three wave mixing (section 2).

One of the ways in which this can be used is to determine the quantum efficiency of a photo-detector, first demonstrated in 1977 [iii] and corroborated by other groups since then [iv, v]. A brief discussion about terminology would be useful here. Quantum efficiency usually refers to the efficiency with which a photodiode converts incident photons to electrons. In the case of, say, an avalanche photo-detector (APD), the situation is complicated by the existence of gain in the device. Added to this there is the transfer function of the electronics of the detector and any counting units. In this

dissertation and in much of the literature concerning the techniques described here, QE is considered in a more general way, which could be described as the photon detection efficiency (PDE) of a photon detection module. In practice, this may also include any filters or focussing lenses used. In particular, the manufacturers of the APDs used in our experiments specify QE for the APD head and PDE including the electronics.

Two detectors, *A* and *B* say, are used in this arrangement and aligned to intercept the downconverted pairs so that if a photon arrives at one detector, its twin should arrive at the other. Every time there is a count on one detector, say *A*, it can be asked if there is a corresponding count on *B*. The number of coincidences will then be the quantum efficiency of *B* times the number of counts on *A*. This has the advantage over conventional methods in that a calibrated source is not needed, the measurement is absolute and can be performed with uncalibrated detectors.

A second application is the measurement of the spectral radiance of a light source, demonstrated by Migdall *et al* [vi]. In the previous case, the downconverted photons were produced spontaneously. However, PDC can be stimulated by injecting a source of photons with the same energy and momentum as one of the downconverted photons, the signal, say. In this arrangement, the system is a parametric amplifier with energy from the pump being converted into the signal and idler fields. The radiance of the source can then be measured from the increase in the number of idler photons.

The attractive feature of this method emerges when the stimulated output is compared to the spontaneous output with the source shuttered. The spontaneous

downconversion can be considered to be stimulated by the background vacuum fluctuations of one photon per mode. This means that the spectral radiance of the source can be expressed in terms of photons per mode, which in turn is expressible in terms of fundamental constants. Essentially, the vacuum fluctuations are being used as a measurement standard - a standard that is clearly universal. One technical advantage of this is that, if the source is in the infrared, it can be arranged to have the idler in the visible where the detection technology is more advanced.

Current work on QE and spectral radiance measurements has realised uncertainties of the order of 0.5% [v, vii, viii] and 1% [vi, ix] respectively. Ongoing research is investigating how these uncertainties may be reduced in order to make the use of correlated photons a viable technique. After reviewing the theory of parametric downconversion in section 2, measurements of QE conducted at NPL are reported in section 3, in which an uncertainty of ~0.5% was achieved. In section 4, a proposed plan for spectral radiance measurement is described and the possible sources of uncertainty discussed.

2. Parametric down-conversion

The phase matching conditions (1.1) can be derived through a classical analysis in which PDC is viewed as a three-wave mixing process where coupling between the fields arises due to the nonlinear polarisation of the medium. As shall be seen, whilst the classical analysis predicts the growth of the signal and idler fields, it does not account for the spontaneous downconversion that seeds the process in the first place. For this, a quantum mechanical account is needed.

First, a classical analysis is followed in order to gain some insight into how PDC depends on the nonlinear polarisation. The argument follows along similar lines to the analysis of second harmonic generation given in [x].

2.1 PDC as three wave mixing

We start by assuming the frequency components of the field are plane waves of the form

$$\mathbf{E}(\omega,\mathbf{r}) = \mathbf{A}(\omega,\mathbf{r})\exp(i\mathbf{k}\cdot\mathbf{r}) \tag{2.1}$$

where $\mathbf{E}(\omega, \mathbf{r})$ is the electric field, $\mathbf{A}(\omega, \mathbf{r})$ is the amplitude and $\mathbf{r}$ is the position vector. Adopting the slowly varying envelope approximation, we can write the nonlinear wave equation (in the frequency domain) as

$$\mathbf{k}\cdot\nabla\mathbf{A}(\omega,\mathbf{r}) = \frac{i\omega\mu_0}{2}\mathbf{P}^{NL}(\omega,\mathbf{r})\exp(-i\mathbf{k}\cdot\mathbf{r}) \tag{2.2}$$

where μ_0 is the permeability of free space and $\mathbf{P}^{NL}(\omega, \mathbf{r})$ is the nonlinear polarisation. In the case of PDC, we are only concerned with the second order nonlinear polarisation $\mathbf{P}^{(2)}(\omega, \mathbf{r})$, given by [x]

$$\mathbf{P}^{(2)}(\omega,\mathbf{r}) = \varepsilon_0\chi^{(2)}(\omega;\omega_1,\omega_2)\mathbf{E}(\omega_1,\mathbf{r})\mathbf{E}(\omega_2,\mathbf{r}) \tag{2.3}$$

where ε_0 is the permittivity of free space and $\chi^{(2)}(\omega; \omega_1, \omega_2)$ is the second order susceptibility tensor. The argument of $\chi^{(2)}$ indicates that ω is the resultant of the components at ω_1 and ω_2. So, using (2.1), for the signal frequency, we have

$$\mathbf{P}^{(2)}(\omega_s, \mathbf{r}) = \varepsilon_0 \chi^{(2)}(\omega_s; \omega_p, -\omega_i) \mathbf{A}(\omega_p, \mathbf{r}) \mathbf{A}^*(\omega_i, \mathbf{r}) \exp(i(k_p - k_i) \cdot \mathbf{r}) \tag{2.4}$$

with a similar expression for the idler frequency.

Equation (2.4) can put into scalar form by expressing the second order polarisation component in a particular direction in terms of an *effective nonlinearity*, d_{eff} (see section 2.4). We then have

$$P^{(2)}(\omega_s, \mathbf{r}) = \varepsilon_0 d_{eff} A_p(z) A_i^*(z) \exp(i(k_p - k_i) \cdot \mathbf{r}) \tag{2.5}$$

where the frequency dependence of the amplitudes is now implied by subscripts to simplify the notation. Substituting (2.5) into (2.2) and taking the direction of propagation to be along the z-axis, gives, for both the signal and the idler, the coupled equations

$$\begin{aligned} \frac{\partial A_s(z)}{\partial z} &= \gamma_s A_i^*(z) \exp(-i \Delta k z) \\ \frac{\partial A_i^*(z)}{\partial z} &= -\gamma_i A_s(z) \exp(-i \Delta k z) \end{aligned} \tag{2.6}$$

where

$$\gamma_s = \frac{\omega_s^2 d_{eff}}{2k_s} A_p A_i^* e^{i\Delta k z}$$
$$\gamma_i = \frac{\omega_i^2 d_{eff}}{2k_i} A_p A_s^* e^{i\Delta k z} \tag{2.7}$$

and

$$\Delta k = k_p - k_s - k_i. \tag{2.8}$$

We are assuming that the pump is not depleted, so $A_p(z)$ is taken as a constant. Comparison with the second equation of (1.1) shows that the phase mismatch term, Δk, is just a restatement of the conservation of momentum. Had this analysis been performed in the temporal domain, the conservation of energy would also have emerged.

Solving equations (2.6) with the boundary conditions $A_s(0) = A_{s0}$, $A_i(0) = A_{i0}$ and putting $\Delta k = 0$, we arrive at

$$A_s(z) = A_{s0}\cosh(gz) + \left(\frac{\gamma_s}{g}\right) A_{i0}^* \sinh(gz)$$
$$A_i(z) = A_{i0}^*\cosh(gz) - \left(\frac{\gamma_i}{g}\right) A_{s0} \sinh(gz) \tag{2.9}$$

where the gain term, g, is given by

$$g^2 = \gamma_s \gamma_i$$
$$= \frac{\omega_s \omega_i d_{eff}^2 I_p}{4c^2 n_s n_i} \tag{2.10}$$

c is the speed of light and n_s, n_i are the refractive indices seen by the signal and idler respectively. Converting (2.9) into intensities, averaging to eliminate the phase-dependent term and using the relation $|\gamma_s/\gamma_i| = n_i\omega_s/n_s\omega_i$, we arrive at an expression for the mean number densities of the photons in the downconverted fields

$$\begin{aligned} N_s &= \sinh^2 gz + \cosh^2 gz \\ N_i &= \sinh^2 gz + \cosh^2 gz \end{aligned} \quad \text{(classical result)} \qquad (2.11)$$

As we shall see, the quantum mechanical result will have a subtle but important difference.

2.2 Quantum mechanical analysis

A quantum mechanical model of parametric processes was developed in 1961 by Louisell *et al* [xi]. The Hamiltonian of the modes in the nonlinear medium can be written

$$\begin{aligned} H &= \frac{1}{2}\int_V \mathbf{D}\cdot\mathbf{E} + \mathbf{B}\cdot\mathbf{H}\,\mathrm{d}V \\ &= \frac{1}{2}\int_V \varepsilon_0\varepsilon\cdot\mathbf{E} + \mathbf{B}\cdot\mathbf{H}\,\mathrm{d}V + \frac{1}{2}\int_V \mathbf{P}^{(2)}\cdot\mathbf{E}\,\mathrm{d}V \end{aligned} \qquad (2.12)$$

so that the second term, involving the second order polarisation, is treated as a perturbation. After quantizing, the growth of the downconverted fields is described by creation and annihilation operators, $a^\dagger_k(t)$ and $a_k(t)$, such that, at $t = 0$

$$a_{k0}^{\dagger} a_{k0} |N_{k0}\rangle = \nu_{k0} |N_{k0}\rangle \tag{2.13}$$

where N_{k0} is the number of photons in the kth mode and $|N_{k0}>$ denotes the state with this eigenvalue. The operators $a^{\dagger}_k$ and a_k are so named because they transform the N_{k0} states into $N_{k0} + 1$ and $N_{k0} - 1$ states respectively. A significant aspect of the quantum mechanical treatment arises because $a^{\dagger}$ and a obey the commutation relations

$$\begin{aligned} [a_j, a_k^{\dagger}] &= \delta_{jk} \\ [a_j, a_k] &= [a_j^{\dagger}, a_k^{\dagger}] = 0 \end{aligned} \tag{2.14}$$

Denoting the signal and idler fields by the subscripts s and i as before, the time dependent solutions for $a^{\dagger}$ and a can be written, according to [vi], as

$$\begin{aligned} a_s &= \exp(-i\omega_s t) a_{s0} \cosh\kappa + \exp(-i\phi) a_{i0}^{\dagger} \sinh\kappa \\ a_i^{\dagger} &= \exp(i\omega_i t) a_{i0}^{\dagger} \cosh\kappa - \exp(i\phi) a_{s0}^{\dagger} \sinh\kappa \end{aligned} \tag{2.15}$$

where κ is a gain coefficient and ϕ is a phase term introduced by the pump. Calculating the expectation values of the photon number operators given in (2.13), we have

$$\begin{aligned} \langle N_s \rangle &= \nu_{s0} \cosh^2\kappa + (1 + N_{i0}) \sinh^2\kappa \\ \langle N_i \rangle &= \nu_{i0} \cosh^2\kappa + (1 + N_{s0}) \sinh^2\kappa \end{aligned} \tag{2.16}$$

Comparing this result to (2.11), derived from the classical analysis, we see that, apart from now being in the time domain, (2.16) predicts the growth of the signal and idler

fields even if the initial number densities are zero, due to the unity terms. These terms are a direct result of the commutation relations (2.14) and correspond to spontaneous downconversion. Since the dimensions of (2.16) are photons per mode, we interpret the spontaneous downconversion as in fact being *stimulated* by one photon per mode due to vacuum fluctuations. In section 4.1, we shall see how this result enables us to make spectral radiance measurements in terms of fundamental constants.

2.3 Phase matching

In order to meet the phase matching conditions (1.1), we need to exploit the birefringent properties of the nonlinear medium. In general, PDC is usually only possible in two cases, which we call Type I and Type II. With Type I downconversion, a wave polarised along a fast axis gives rise to two waves polarised along a slow axis. In Type II, a fast pump wave decays to a fast and a slow wave. These are summarised in Table 2-1 below for biaxial and uniaxial crystals.

Table 2-1 *Types of parametric downconversion. The letters 'e' and 'o' stand for extraordinary and ordinary respectively.*

	Biaxial	Positive uniaxial	Negative uniaxial
Type I	*fast* → *slow* + *slow*	*o* → *e* + *e*	*e* → *o* + *o*
Type II	*fast* → *fast* + *slow*	*o* → *e* + *o*	*e* → *e* + *o*

In our experiments, we use barium beta-borate crystal (BBO), which is negative uniaxial, and so we confine the following discussion to this category of nonlinear crystal.

For Type I downconversion, the daughter photons are emitted on light cones coaxial with the pump beam (see Figure 2-1). Since momentum is conserved, correlated pairs occur diametrically opposite each other on their respective cones.

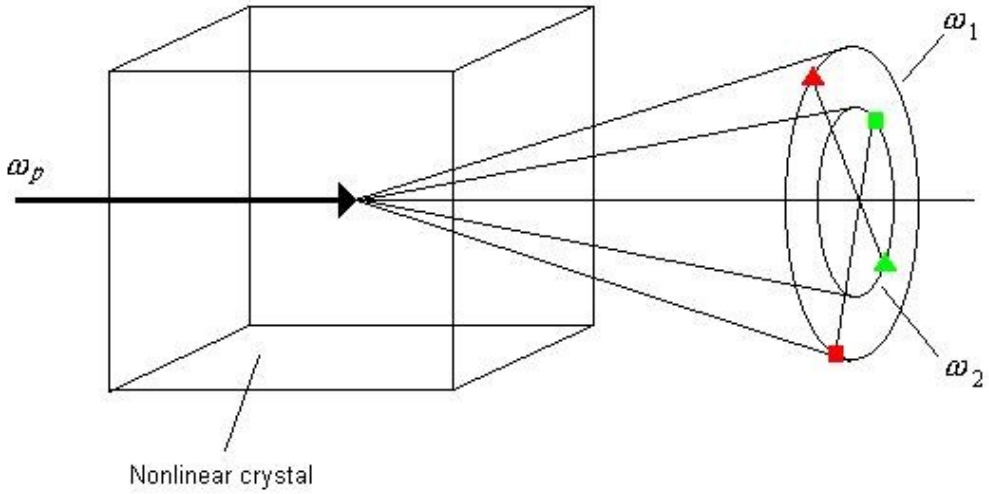

Figure 2-1. *Type I downconversion for a negative uniaxial crystal. The pump wave is incident from the left. The squares and triangles mark typical positions of conjugate pairs of correlated photons.*

With Type II downconversion, the refractive index of the extraordinary wave depends on the angle between its direction of propagation and the optic axis. Hence, the light cones are no longer coaxial. Figure 2-2 illustrates Type II downconversion in the general case and in the particular case of collinear downconversion where the daughter photons can be emitted in the same direction as the pump.

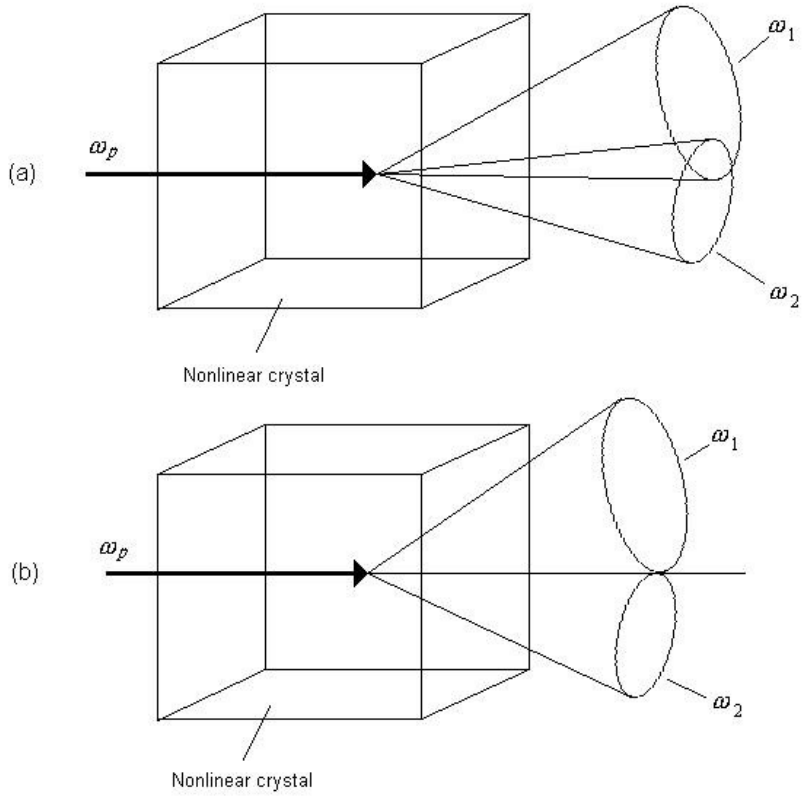

Figure 2-2 *(a) Type II down conversion for a negative uniaxial crystal. The optic axis lies in the plane of the paper. (b) The collinear case where, at the point where the two light cones touch, the downconverted photons are collinear with the pump photon.*

In order to calculate the phase matching conditions, we note the relationship between the magnitude of the **k** vector and the angular frequency

$$|\mathbf{k}| = \frac{n(\theta,\omega)\omega}{c} \tag{2.17}$$

where θ is the angle between the **k** vector and the optic axis. For waves polarised along the ordinary axis, the refractive index, n_o, does not depend on θ. Figure 2-3 illustrates the θ dependence of the extraordinary refractive index $n_e(\theta)$ at a given wavelength. Here n_o and n_e are the semi-major and semi-minor axes respectively of

the projection of the index ellipsoid on to the plane including the optic axis. The wavelength dependence of these refractive indices can be found from appropriate Sellmeier equations (see Appendix A).

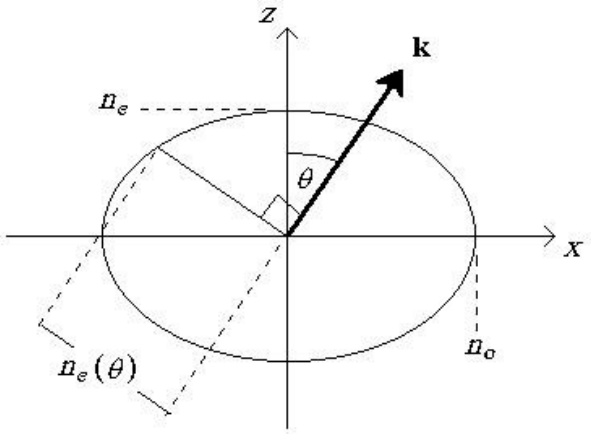

Figure 2-3 *The index ellipsoid for a negative uniaxial crystal (viewed side on from the negative y direction) showing how the extraordinary index of refraction, $n_e(\theta)$, varies with the angle of propagation direction,* **k***, to the optic axis (z axis). n_o is the semi-major axis and n_e is the semi-minor axis.*

Using Figure 2-3 we can find an expression for $n_e(\theta, \omega)$

$$n_e(\theta,\omega) = n_e(\omega) n_o(\omega) \left[\frac{1 + \tan^2\theta}{n_e^2(\omega) + n_o^2(\omega)\tan^2\theta} \right]^{1} \tag{2.18}$$

Finally, by expressing the **k** vectors of the signal and idler with respect to the pump beam as illustrated in Figure 2-4, the (momentum) phase matching conditions can be written [xii]

$$\left|\mathbf{k}_p\right|^2 - \left|\mathbf{k}_2\right|^2 - \left|\mathbf{k}_p\right|\left|\mathbf{k}_1\right|\cos\alpha + \left|\mathbf{k}_1\right|^2 = 0 \tag{2.19}$$

where α_1 is the angle between the $\mathbf{k}_1$ vector and the pump. Here, the ω and θ dependences have not been made explicit in order for (2.19) to be appropriate for both Type I and Type II downconversion. It must be remembered, however, that $|\mathbf{k}_p|$ will depend on θ_p, the angle between the pump and the optic axis. Moreover, for Type II downconversion, $|\mathbf{k}_1|$ (which we take to be the extraordinary wave) will depend on the angle between $\mathbf{k}_1$ and the optic axis, θ_1, which in turn depends on α_1 and the angle of rotation around the pump beam ϕ. In this case, (2.19) must be solved numerically (see Appendix B). Clearly, α_2 is simply related to α_1 by

$$|\mathbf{k}_1|\sin\alpha = |\mathbf{k}_2|\sin\alpha \tag{2.20}$$

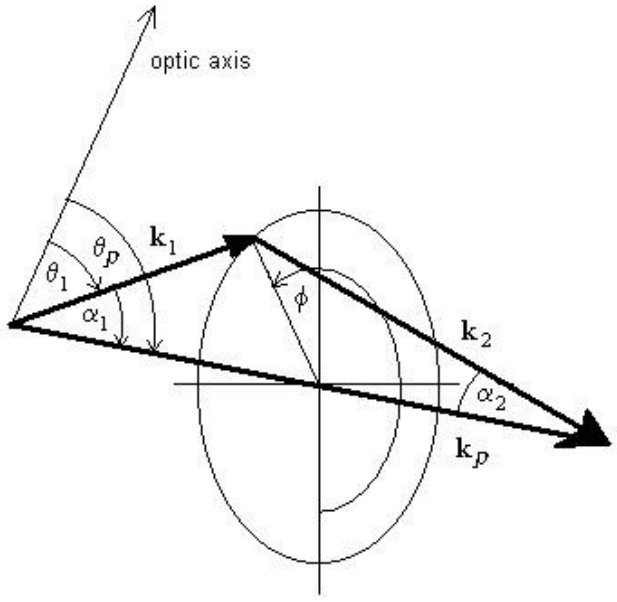

Figure 2-4 *Vector representation of phase matching. Angles shown are those within the crystal. The magnitude of* $\mathbf{k}_p$ *depends on the angle* θ_p*. For Type II downconversion (taking* $\mathbf{k}_1$ *as the extraordinary wave), the magnitude of* $\mathbf{k}_1$ *will depend on the angle* θ_1*. In the pump reference frame, the x-axis points downwards, the y-axis points to the right and* ϕ *is the azimuthal angle around the pump. (Figure adapted from reference [xii]).*

The angles indicated in Figure 2-4 and used above are those inside the crystal. To calculate the half angles of the light cones that emerge from the crystal, we apply Snell's law (which is a simple matter if the pump beam is normal to the crystal surface). Figure 2-5 shows actual photographs of the light cones for BBO, whilst Figure 2-6 indicates the theoretically predicted cone angles for three wavelengths. Note that the central yellow spot due to the fluorescence on the UV blocking filter originates at a point after the downconversion and so would move relative to the light cones as the camera position was moved.

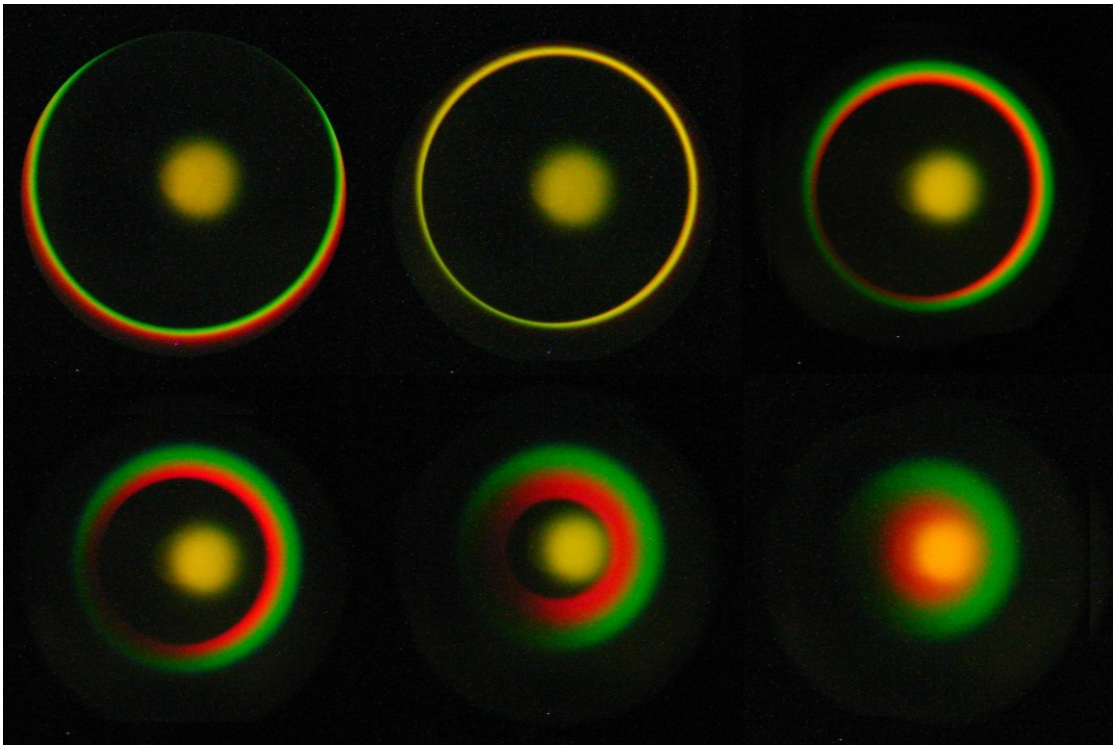

Figure 2-5 *Photographs of parametric downconversion in BBO with the optic axis at 35° to the normal and pumping at 351.1 nm. The sequence of pictures shows the crystal being rotated through plus and minus 6°. Thus, in the top left hand picture, the pump is making an angle of 41° with the optic axis, in the bottom right, an angle of 29°. The top right hand picture shows normal incidence. The bright yellow patch in the centre of each picture is due to fluorescence on the UV filter used to block the pump radiation. The photographs were obtained by imaging the light cones through a lens on to a digital camera.*

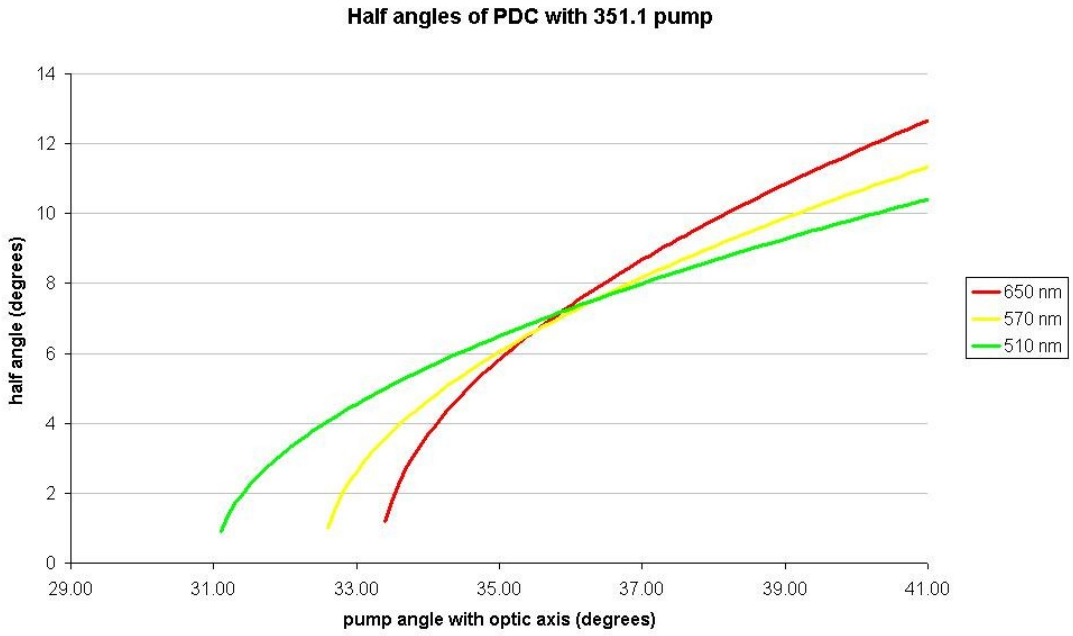

Figure 2-6 *Calculations of the cone angles at different wavelengths against the angle of the pump with the optic axis. Note the cross over point for the colours, which is also seen in the photographs in Figure 2-5.*

2.4 The effective nonlinearity

In section 2.1 we introduced the effective nonlinearity d_{eff}. In this section we derive expressions for d_{eff} for the processes of Type I and Type II downconversion in BBO. We start by noting that, due to the commutativity of the electric field vectors, the second order susceptibility tensor can be reduced to an 18-element **d**-tensor. The form of the **d**-tensor can usually be simplified by examining the crystal symmetries of the nonlinear medium in question. If, in addition, Kleinman symmetry [xiii] holds, i.e. the nonlinear medium is transparent in the spectral region of interest, then further simplifications can be applied.

For BBO, the crystal symmetry and point group is Trigonal, 3m. For our purposes, we shall be interested in a spectral range from around 300 nm to the near infrared. According to the Sellmeier equations used in Appendix A, the nearest resonances of BBO are around 130 nm and 9.5 μm, so we are justified in applying Kleinman symmetry. In this case, the **d**-tensor is [x]

$$\mathbf{d} = \begin{bmatrix} 0 & 0 & 0 & 0 & d_{15} & \overline{d_{22}} \\ \overline{d_{22}} & d_{22} & 0 & d_{15} & 0 & 0 \\ d_{15} & d_{15} & d_{33} & 0 & 0 & 0 \end{bmatrix} \tag{2.21}$$

where the over-bars indicate negation. The ω component of the polarisation is now given by

$$\mathbf{P}^{(2)}(\omega) = \mathbf{d} : \mathbf{E}(\omega_1)\mathbf{E}(\omega_2) \tag{2.22}$$

where, after making the **r** dependence implicit, the second order electric field tensor can written out as

$$\mathbf{E}(\omega)\tilde{\mathbf{E}}(\omega) = \begin{bmatrix} E_{1x}E_{2x} \\ E_{1y}E_{2y} \\ E_{1z}E_{2z} \\ E_{1y}E_{2z} + E_{2y}E_{1z} \\ E_{1x}E_{2z} + E_{2x}E_{1z} \\ E_{1x}E_{2y} + E_{2x}E_{1y} \end{bmatrix} \tag{2.23}$$

We now take the dot product of (2.22) with the unit vector in the direction of polarisation for the frequency component we are interested in (with (2.23) consisting of the mixing terms for the other two components). Figure 2-7 shows the pump and downconverted wave vectors (1 and 2) in relation to the crystal axes, z being the optic axis. For extraordinary waves, the polarisation will be in the plane defined by the optic axis and the wave vector. The polarisation of ordinary waves will be perpendicular to this plane.

Thus, for Type I downconversion, the polarisation unit vectors for each field will be

$$\begin{aligned} \mathbf{e}_1 &= \sin\phi_1\mathbf{e}_x - \cos\phi_1\mathbf{e}_y \\ \mathbf{e}_2 &= \sin\phi_2\mathbf{e}_x - \cos\phi_2\mathbf{e}_y \\ \mathbf{e}_p &= -\cos\theta_p\cos\phi_p\mathbf{e}_x - \cos\theta_p\sin\phi_p\mathbf{e}_y + \sin\theta_p \end{aligned} \tag{2.24}$$

where the magnitudes of each field will be E_1, E_2 and E_p. Taking the E_2 to be the field of interest, we find

$$\mathbf{e}_2 \cdot \mathbf{P}^{(2)}(\omega\ \mathbf{r}) = \varepsilon_0 d_{eff} E_1 E_p \tag{2.25}$$

where the effective nonlinearity is

$$d_{eff} = d_{15}\sin\theta_e \cos(\phi_1 - \phi_2) - d_{22}\cos\theta_e \sin(\phi_1 + \phi_2 + \phi_p) \qquad \text{(Type I)} \tag{2.26}$$

Clearly, since interchange of subscripts 1 and 2 makes no difference, we have the same result for either ordinary wave.

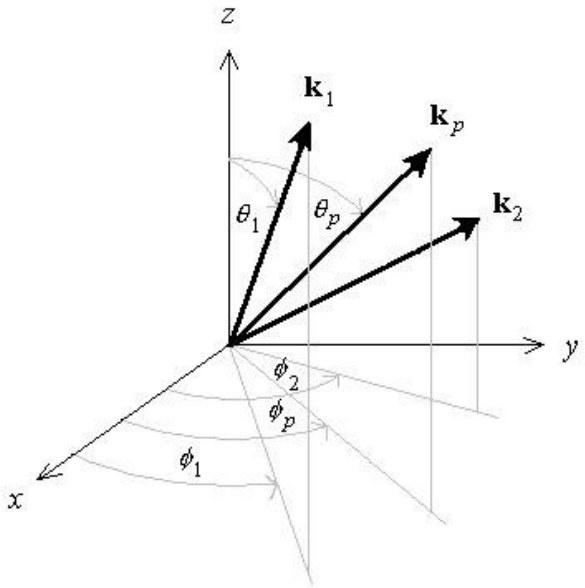

Figure 2-7 *The wave vectors for the pump (p) , signal and idler (1 and 2) shown in relation to the crystal axes (z is the optic axis)*

In the case where all the waves and the optic axis are coplanar, $\phi_1 = \phi_2 = \phi_p$ and we have

$$d_{eff} = d_{15}\sin\theta_e - d_{22}\cos\theta_e \sin 3\phi_e \qquad \text{(Type I)} \tag{2.27}$$

as quoted in [x]. Note that as $d_{15} = d_{31}$ (when Kleinman Symmetry is valid), some authors (for instance [xiv]) write the above expression with d_{31} in place of d_{15}. A further notational complication arises since there is not universal agreement about the orientation of the crystal *x*-*y* axes. Some authors have these rotated by 90º relative to those used above. This requires a transformation of the **d** tensor and (2.27) becomes [xv]

$$d_{eff} = d'_{31}\sin\theta_p - d'_{11}\cos\theta_p\cos 3\phi_p \qquad \text{(Type I) (alternative)} \qquad (2.28)$$

where $d'_{31} = d_{31} = d_{15}$, $d'_{11} = d_{22}$ and $\phi'_p = \phi_p - 90°$.

For Type II downconversion we take $\mathbf{k}_1$ to be the extraordinary wave. The unit vectors are now

$$\begin{aligned}
\mathbf{e}_1 &= \cos\theta_1\cos\phi_1\mathbf{e}_x - \cos\theta_1\sin\phi_1\mathbf{e}_y + \sin\theta_1 \\
\mathbf{e}_2 &= \sin\phi_2\mathbf{e}_x - \cos\phi_2\mathbf{e}_y \\
\mathbf{e}_p &= \cos\theta_p\cos\phi_p\mathbf{e}_x - \cos\theta_p\sin\phi_p\mathbf{e}_y + \sin\theta_p
\end{aligned} \qquad (2.29)$$

which gives

$$\begin{aligned}
d_{eff} = {} & d_{15}\{\cos\theta_1\sin\theta_p\sin(\phi_1 - \phi_2) + \cos\theta_p\sin\theta_1\sin(\phi_p - \phi_2)\} \\
& + d_{22}\cos\theta_1\cos\theta_p\cos(\phi_1 + \phi_2 + \phi_p)
\end{aligned} \qquad \text{(Type II)} \qquad (2.30)$$

(we get the same result for both downconverted waves, although this is not obvious from the maths). If we once more take the wave vectors and optic axis to be coplanar, we arrive at the result often given in nonlinear optics literature

$$d_{eff} = {}^{l}_{22} \cos^2 \theta_{r} \cos 3\phi_{r}, \qquad \text{(Type II)} \tag{2.31}$$

Again, alternative notation exists.

To solve equations (2.26) and (2.30), we first need to solve the phase matching equations (2.19) and (2.20) for α_1 and α_2. We can then transform from the pump frame of reference (Figure 2-4) to the crystal frame (Figure 2-7) for each wave to find the required angles.

3. Quantum efficiency measurements

3.1 Measurement of quantum efficiency

Since the downconverted photons are produced in pairs, the existence of one implies the existence of the other. As the energies and momenta of both photons are correlated, if we detect one of them at a particular point, we can predict where its twin should be at that time. We can exploit this fact to measure the quantum efficiencies of photodetectors, illustrated schematically in Figure 3-1.

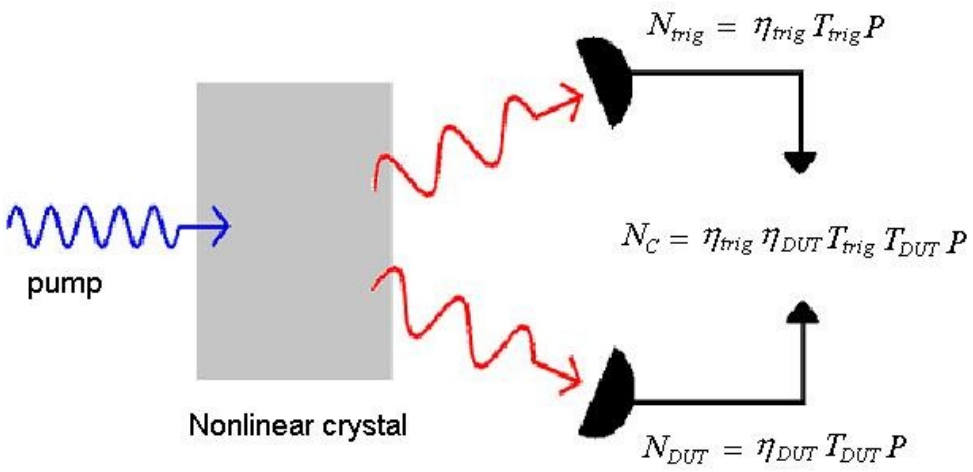

Figure 3-1 *Schematic of quantum efficiency measurements using parametric downconversion. (Adapted from [xvi]).*

Consider each twin of the downconverted photon pairs being sent to different detectors, which we will refer to as the *trigger* and the *device under test* (DUT). Each detector will record a certain number of the correlated photons

$$N_{trig} = \eta_{trig} T_{trig} P$$
and
$$N_{DUT} = \eta_{DUT} T_{DUT} P \qquad (3.1)$$

where $\eta_{trigger}$ and η_{DUT} are the quantum efficiencies, T_{trig} and T_{DUT} are the total transmittances of each channel and P is the number of generated pairs. Every time we detect a photon on the trigger we can ask whether we also detected a photon on the DUT. Since we are restricting our attention to the subset of the total number of photon pairs that make up the trigger count, the number of coincidence counts, N_C, that we detect in this way is

$$N_C = \eta_{trig}\eta_{DUT}T_{trig}T_{DUT}P \tag{3.2}$$

If we know N_{trig}, it is a straightforward task to calculate the quantum efficiency of the DUT

$$\eta_{DUT} = \frac{N_C}{T_{DUT}N_{trig}} \tag{3.3}$$

In practice, N_C will be increased by stray photons and dark counts. Similarly, the total trigger counts will include extra counts, giving rise to false triggers, which must be subtracted from N_{trig}. Denoting these extra counts by N_{acc} and N_{false} respectively, we can re-write (3.3) as

$$\eta_{DUT} = \frac{N_C - N_{acc}}{T_{DUT}(N_{trig} - N_{false})} \tag{3.4}$$

3.2 Sources of uncertainty

In assessing the accuracy of this method, the sources of uncertainty need to be addressed. The fractional uncertainty in η_{DUT} is given by

$$\frac{\Delta\eta_{DUT}}{\eta_{DUT}} = \left[\frac{\Delta N_C^2 + \Delta N_{acc}^2}{(N_C - N_{acc})^2} + \frac{\Delta N_{false}^2}{(N_{trig} - N_{false})^2} + \frac{\Delta T_{DUT}^2}{T_{DUT}^2} \right]^{1} \tag{3.5}$$

3.2.1 False and accidental counts

The uncertainty in N_{acc} arises because, in practice, we have to estimate this quantity and take an average over several readings. Similarly, as there is fluctuation in the number of coincidence counts over a number of runs, N_C must also be arrived at through averaging. The number of false counts must be extrapolated from the counts per second with no PDC to the counts expected over the time it takes to register a given number of triggers. Note that, in our experiment, since the number of triggers that we count for is fixed, the uncertainty in N_{trig} is zero.

If we assume that the photon arrival times are Poisson distributed, then we can take the square roots of the means to be the uncertainties. However, in our experiments, the stray light is due principally to fluorescence from the UV laser and downconversion at other wavelengths. Both of these sources depend on the intensity of the laser, so ΔN_{acc}, ΔN_C and ΔN_{false} may be affected by the laser stability. However, with the laser light stabilised, this should not be a major problem and assuming the uncertainties remain proportional to the square roots of the means, the contributions

of these fractional uncertainties become smaller as the number of trigger counts (and consequently the coincidence, accidental and false counts) is increased.

3.2.2 Uncertainties in transmission

The transmittance, T_{DUT}, includes the optical losses in the crystal, filters and focussing optics as well as any loss of downconverted photons on the DUT due to misalignment. The uncertainty, ΔT_{DUT}, therefore depends on how accurately these losses can be specified.

3.2.2.1. Losses in the crystal

Losses in the crystal arise through reflection on the output face of the crystal, absorption in the medium, and scattering. The first of these can be alleviated through the use of anti-reflection coatings at the wavelength of the downconverted light. For low reflectances, the transmittance from the centre of the crystal can be approximated to the square root of the total transmittance. Calculations show [xvii] that, from the centre of the crystal, this approximation is accurate to 0.01% or better if the reflectances at both faces are similar.

3.2.2.2. Losses in optical elements

Filters were used to pass the downconverted light whilst blocking any stray light, due primarily to fluorescence. Lenses were also required to focus the light on to the detector active areas. At present, laser techniques have achieved accuracies of 0.01% to 0.02% for the transmittance measurements of spectral filters (at NPL) and 0.02% for lenses [xviii].

Table 3-1 summarises the currently achievable measurement uncertainties in the visible region. The figures are taken from [xvii] and are based on work undertaken at NPL. The figures suggest that overall uncertainties due to optical losses can be as low as 0.05%.

Table 3-1 *Measurement uncertainties currently achievable (taken from ref [xvii])*

		Measurement uncertainties (%)		
		Grating spectrometer	CW laser	Pulsed laser
Crystal	transmittance	0.03	0.005	0.01
	absorption	0.08	0.01	0.02
	scatter	-	0.005?	?
Filters	transmittance	0.03	0.005	0.02
Lenses	transmittance	-	0.02	?

3.2.2.3. Geometric and spectral misalignment

We need to ensure that the twins of all correlated photons at the wavelength of interest incident on the trigger are also incident on the DUT. Reasons why this may fail to be the case are geometric misalignment; poor focussing on to the detector active areas or poor spectral overlap on the filters used. In practice, we can improve the overlap between the detectors by making the trigger subtend a smaller angle from the PDC source, either by use of a narrower aperture or by physically placing the detector further from the crystal. In our set-up, the detectors are both mounted on automated stages, which facilitates systematic fine-tuning of the alignment by maximising the coincidence counts. The alignment of the DUT with respect to the lens can also be adjusted remotely to improve the focussing. We must also contend

with the fact that the PDC does not arise from a point source but takes place over an extended area. The use of thinner crystals can alleviate this.

Since the wavelengths of the downconverted photons define the half cone angle with respect to the pump beam, the use of filters may seem superfluous. However, spectral selectivity is useful in reducing false triggers, which are due to the fluorescence at the crystal and the spread of downconverted light around the wavelength of interest (see Figure 2-5). Using a filter over the DUT may not be necessary if we can subtract the accidental counts accurately from the coincidences. This is admissible providing the contribution to the uncertainties due to the standard deviation of the accidental counts is negligible. If a filter is used, we need to ensure that its transmission bandwidth encompasses that of the trigger filter. Figure 3-7 shows the transmittance curves of the filters used in these experiments.

Quantifying the uncertainty due to geometric misalignment is somewhat difficult. Having made our experimental apparatus as robust as possible and taken the steps outlined above to minimise the error, we might assume initially that this uncertainty is negligible. Ultimately, it will be the reproducibility and repeatability of the measurements that will determine whether this is so.

3.2.3 Other uncertainties

Not included in (3.5) are any uncertainties due to systematic errors that might be introduced by the particular experimental set up or contingent software and electronics. In our experiments, we found that impedance mismatching on the coincidence counters created reflections in the BNC cables, giving rise to additional counts. This is not a particular problem so long as the reflections do not occur so

rapidly as to overlap with the coincidence peak. However, their presence must still be taken into account when summing the coincidence counts as they may produce a much greater background reading. The technical aspects of this problem are discussed in the next section.

3.3 Experimental set up

The experimental set up for the quantum efficiency measurements is shown in Figure 3-2. An argon ion laser provides vertically polarised pump photons at 351.1 nm. In our set up, the beam is passed through a narrow band pass UV filter (351.1 nm, which excludes any plasma radiation from the laser) into an enclosed box (providing a light tight environment for the experimental apparatus) and reflected by three mirrors to bring it on line with the optical rail, resulting in a beam with horizontal polarisation. An iris is used to narrow the beam and a polariser to clean out any unwanted vertical components. The downconversion could then be turned on and off by the rotating the polarisation with a half-wave plate.

The BBO crystal is cut with the optic axis at 35º to the normal and aligned so that the optic axis is in the horizontal plane. This gives Type I downconversion for the degenerate case of two ordinarily polarised photons at 702 nm when the pump beam is polarised horizontally. After solving equations (2.19) and (2.20), using the Sellmeier equations for BBO given in Appendix A, both downconverted photons are predicted to emerge on a light cone coaxial with the pump beam with a half angle of 6.1º.

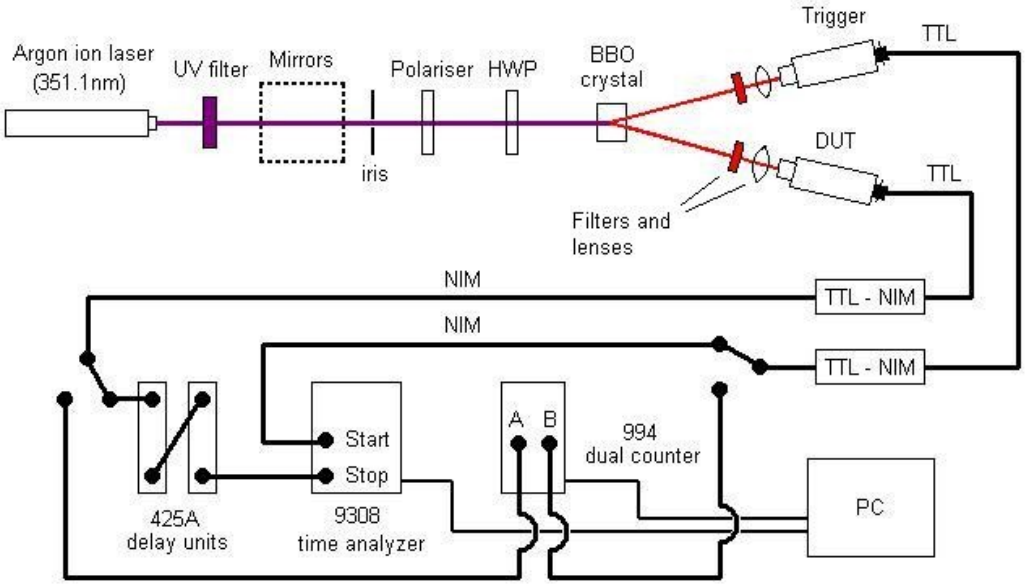

Figure 3-2 *Schematic of the experimental set up for quantum efficiency measurements.*

The detector and lens assemblies are set on plates mounted on *x*, *y*, rotation and tilt stages to allow for alignment to the downconverted beams. The stages are controlled remotely via computer using software written in LabView (Appendix C). Additionally, the detectors themselves are mounted on further *x*, *y* and *z* stages fixed to the plates. In the case of the DUT, these are also automated to allow for spatial mapping and fine tuning the focussing.

In order to reduce the number of stray photons, both detectors are enclosed in light tight boxes and filters are used to select out the required wavelengths. However, in the initial experiments performed, the boxes were not used during alignment as the original designs exceeded the maximum allowed torque on the tilt stages, due to the arrangement of the lens mounts and detectors on the base plates. Subsequently, the boxes were redesigned to achieve a more manageable arrangement and the light tight boxes were used. Photographs of the actual set up can be seen in Appendix D.

Two EG&G SPCM-ARQ series APDs are used as detectors (Appendix E). The output from the trigger is connected to the ‘start’ input of an EG&G Ortec 9308 Picosecond Time Analyzer. This initiates a temporal window, or ‘span’, for counting subsequent events read on the ‘stop’ input. These arrive from the DUT after the signal has been fed through two EG&G Ortec 425A delay units. The units can produce delays of up to 64ns to compensate for the dead time of the 9308, although when the devices were tested, an extra 8 ns delay was found to be added regardless of the setting. This was probably due to the delay in the additional BNC cables required to connect the units. An offset can be set on the 9308 window before subsequent ‘stop’ inputs start to be counted to allow for the delay. Any coincidence counts should be recorded as a narrow peak occurring at a fixed time after the trigger, corresponding to the set delay.

An EG&G Ortec 994 dual counter / timer is used to make independent counts of each channel. Both counters were read remotely via LabView modules incorporated into the software.

The 9308 required NIM inputs whilst the detectors produced TTL pulses. A TTL-NIM converter unit was available but it was not performing properly, so instead, a NIM pulse was simulated by attenuating the signal to 0.8V (measured on an oscilloscope with a 50Ω input impedance) and inverting it to give a negative leading edge. Testing the 9308 with a 0.4V amplitude square wave offset to - 0.4V to reproduce this, we found that we recorded all the stop events at 100kHz. Despite these efforts, a problem still remained with impedance mismatching, leading to pulse reflections. However, the reflections were not excessive and at the time of writing, a

new bespoke TTL-NIM converter unit has been commissioned, which will hopefully rectify the problem.

3.4 Aligning the detectors

3.4.1 Pre-alignment of detectors and lenses

The detectors were initially aligned by eye, positioning them so that they lie on a line at the calculated half cone angle of the PDC from the crystal. An integrating sphere was then placed at the position of the crystal and the lens/detector assemblies adjusted so that the focussed light was under-filling the detector active areas. With the laser on, the PDC can be checked for by imaging the light cone through a lens, enabling concentric red and green rings to be seen (see Figure 2-5). The PDC could be optimised by eye by adjusting the HWP. In the second set of experiments, new lenses were used and the distance to the crystal was increased in order for the PDC to be focussed properly. The distances measured to the filters from the crystal were 119 cm and 146 cm for the DUT and trigger respectively.

3.4.2 Alignment using automated stages

With the BNC cables connected up to the 994 counter, the counts on the trigger detector can be maximised using a LabView routine that moves a given axis around an origin point and plots a graph of the counts. The most effective procedure was found to be as follows. First, the rotation axis is scanned about a degree or so either side of its original position, in increments of 0.1º (usually a degree is sufficient if the alignment by eye was good). The stage is then moved to the angle of maximum count. Next the horizontal (x) and vertical (y) axes are scanned at increments of 0.1mm, the limits being typically a few mm either side of the start point. Again, after each scan, the stages are moved to the maxima. The process is then repeated iteratively with

smaller limits and finer increments until no further improvement can be made. Figure 3-3 shows some typical scans.

At this point, it is useful to check that the half-wave plate is optimised for maximum downconversion. This is done by taking readings with the HWP at different positions and fitting the data to a cosine squared curve.

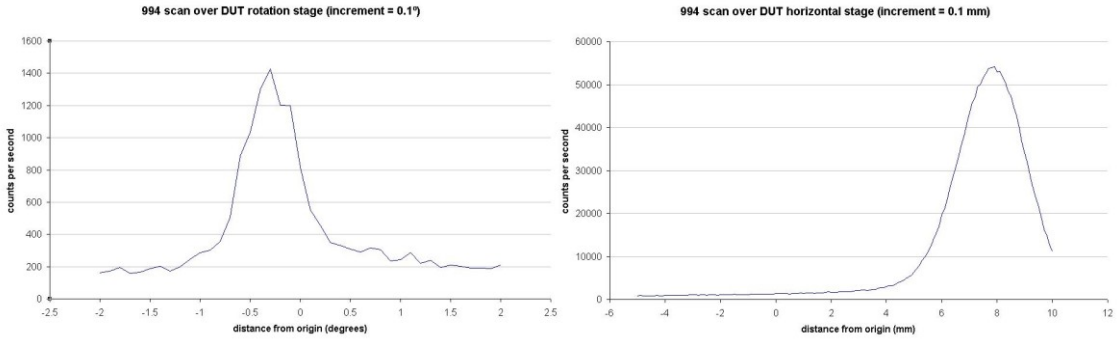

Figure 3-3 *Alignment scans of the DUT axes. On the left is a rotational scan, taken at increments of 0.1°. On the right is a scan over the horizontal axis, with an increment of 0.1 mm. These increments are used on a first scan of an axis.*

With the detectors still connected to the 994 counter, the DUT can be aligned to ensure that it is also seeing downconverted light. Only the first iteration of the above process need be carried out on the 994, since the fine tuning is achieved by connecting to the 9308 and maximising the coincidence counts using a similar procedure.

3.5 BBO transmittance measurements (oblique incidence)

The transmittance of the BBO crystal was measured using the set up shown in Figure 3-4. The Ti-Sapphire laser was mode-locked at 702 nm, with a pulse width on the order of picoseconds. The use of mode locking reduces interference effects from the two faces of the crystal due to the short coherence length of the laser pulses compared to CW [xix]. Since the detectors have been shown not to temporally resolve the

pulses, the output looks like CW. The output light from the laser was vertically polarised.

A half-wave plate was used so that separate measurements could be taken for vertical and horizontal polarisations. Since the principal plane of the BBO crystal (i.e. the plane containing the laser beam direction and the optic axis) was horizontal, polarisation in this plane corresponds to extraordinary (e) waves in the crystal whilst vertical polarisation corresponds to ordinary (o) waves.

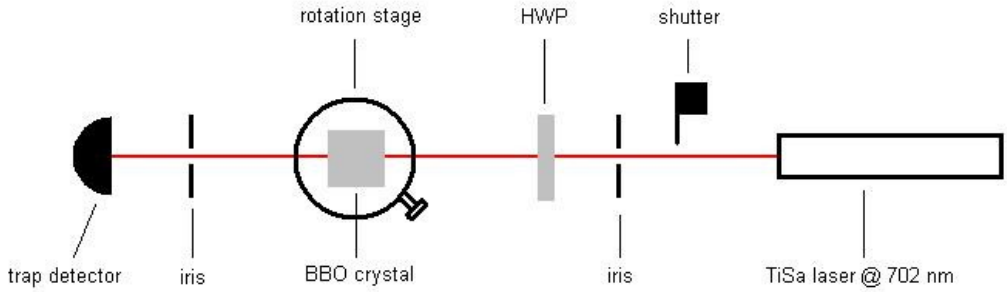

Figure 3-4 *Schematic of the experimental set up for the transmittance measurements.*

The angle of incidence was varied by turning the rotation stage on which the crystal was mounted enabling measurements over a range of angles. The iris following the crystal was used to ensure that the refracted beam did not move off the detector active area.

It was found that there was much greater fluctuation in the detector readings with the HWP in place, probably due to local heating in the plate. This proved to be the greatest source of uncertainty in the measurements and is reflected by the rather large error bars shown in Figure 3-5.

Also shown Figure 3-5 are theoretical predictions for the transmittance of BBO, calculated using the Fresnel equations for the o and e waves (these assume no loss in the crystal). However, the crystal had been given AR coatings on either side: 345-370 nm on the input face and 345-370/600-800 nm on the output face. Unfortunately, details of the coatings were not available and so could not be incorporated into the analysis.

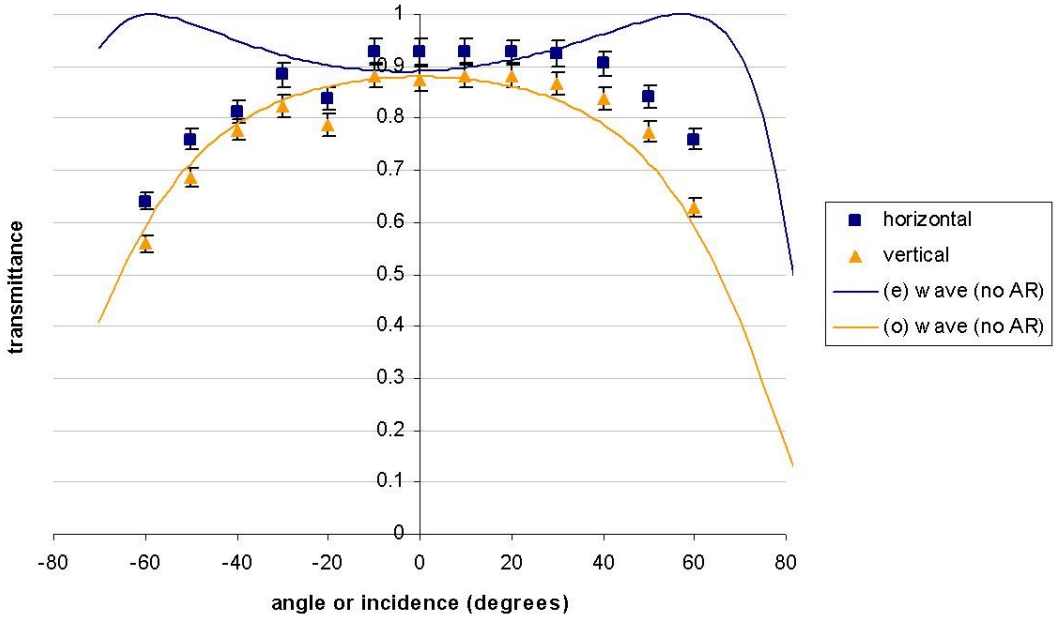

Figure 3-5 *Transmittance through BBO crystal (optic axis lies at 35° to the normal in the horizontal plane. The solid lines show those predicted for the transmittance with no loss or AR coating on the crystal.*

Additional calculations assuming loss and a changing optical path through the crystal due to the rotation did not improve the fit of the theoretical curves. Moreover, for the e wave, the actual transmittance was greater than the theoretical prediction, so a straight-through loss could not be obtained on that basis. So, in the absence of details

of the AR coatings, it was assumed that the transmittance across the media boundaries is unity and that the measurements indicate only loss in the crystal. This gives losses of 0.13 ± 0.02 and 0.07 ± 0.02 for the o and e waves respectively for the measurement at normal incidence.

In order to improve on these results, further measurements would be needed. Since we are principally concerned with the transmittance of downconverted light, we might dispense with the HWP if we can ensure that incident light is vertically polarised (i.e. corresponds to an ordinary ray). Facilities exist at NPL for measuring reflectance, which would enable us to determine the efficacy of the AR coatings empirically.

In previous measurements [xvii] the crystal was mapped into different regions and the normal transmittances found. The transmittance used in practice was assumed to correspond to the central region, found to be 0.9201 ± 0.0002. Although this does not give us an angular dependence (the downconverted light will be emitted at about 6º to the normal), it is the more accurate value and will be used in later calculations.

3.6 Results

In our first set of measurements, the delay unit was set at 64ns, giving a total delay of 72 ns, with the 9308 beginning counts after an offset of 60 ns. However, this arrangement gave rise to a reflection at around 121 ns after the trigger (Figure 3-6 *a*), causing a higher background count. In a subsequent set (Figure 3-6 *b*), the delay was set to 96 ns (giving 104 ns) with a span window of 80 ns, which excluded the reflection. The number of triggers used was 10 000 000 for each run, (Figure 3-6 *b*) showing the average of 8 runs. Measurements were also taken with the filter on the DUT removed. However, in this case the stray light swamped the detector, causing it

to register zero counts at the previous output of the laser (31 mW). With the laser power turned down, the stray light was still found to swamp any coincidence counts.

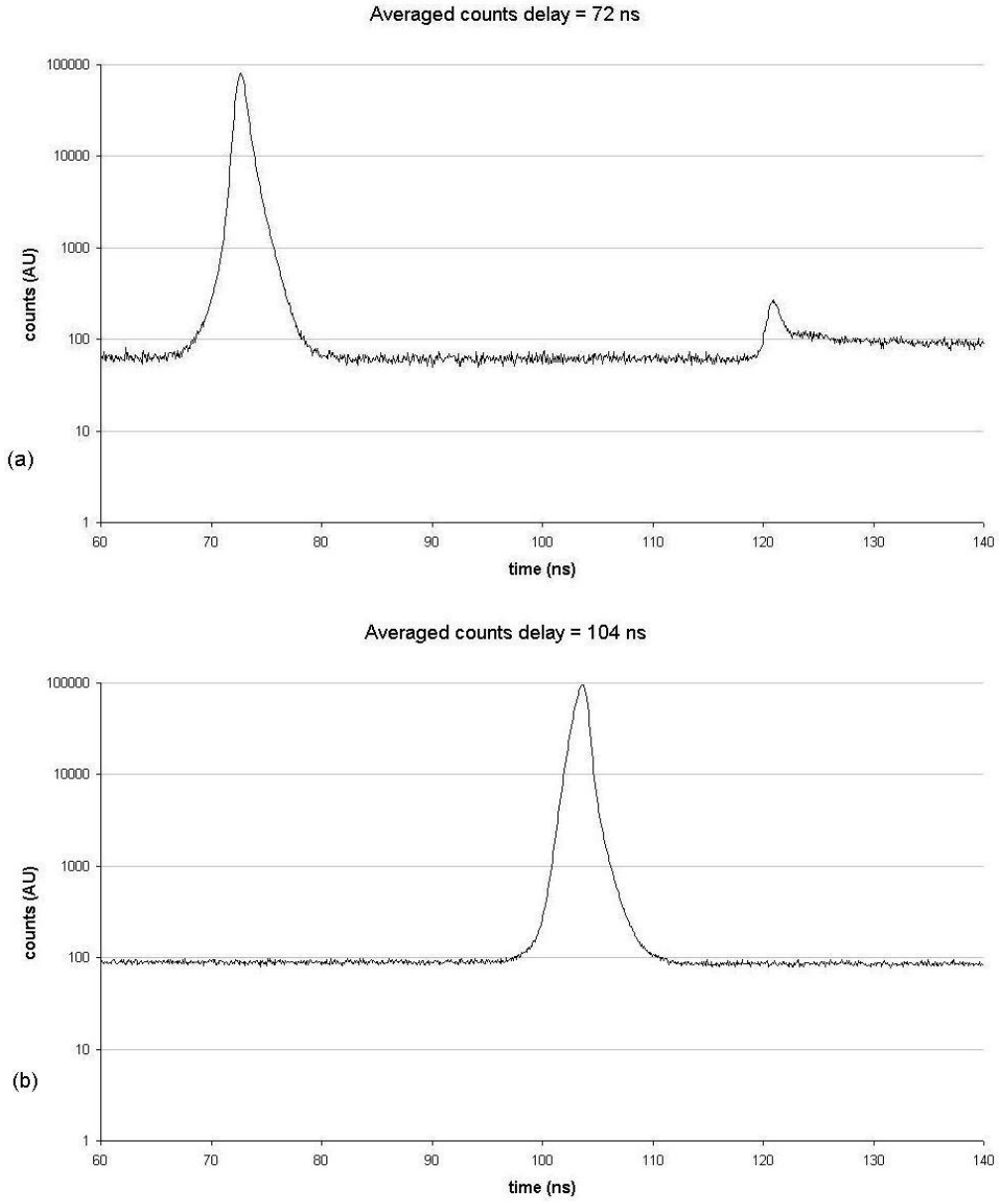

Figure 3-6 *Coincidence counts for the two measurement runs with delays of (a) 72 ns and (b) 104 ns. In both cases, the number of triggers is 10 000 000. The data is averaged over several runs and binned.The higher noise in (a) is due to averaging fewer runs. Note the reflection at around 121 ns in (a). Also note that the ordinate scales are logarithmic.*

3.6.1 Values and uncertainties of photon counts

N_C is calculated by integrating over the coincidence peak, typically over 15 ns either side of the centre. We then integrate a region away from the peak (and any reflection peaks) over the same time span to find the accidental counts. To find the false counts, we first measure the counts per second with the PDC on to calculate how long it would take to generate 10 000 000 triggers. With the PDC off, the false counts per second are found and then multiplied by this time period. As we are assuming that photon arrivals are governed by Poisson statistics, the uncertainty in the false counts (i.e. the standard deviation) is multiplied by the square root of this period.

Table 3-2 and Table 3-3 show results for two separate sets of measurements (the figures for the quantum efficiency are intermediate results without the transmittance of the DUT channel T_{DUT} being corrected for). The measurements took place four days apart and some re-aligning had to be performed on the second set. In the event, this proved only to be a slight adjustment on the rotation stages. In both cases, the laser output was light stabilised at 31 mW. The fractional uncertainties in the QE calculations are 0.07% and 0.09%, as calculated using (3.5).

We note a discrepancy of 0.002 between the measurements. This may be due to such changes in the alignment that different parts of the detector active areas were being irradiated (since these are not in general uniform). Also, the slight change in rotation angle may mean that the PDC is incident at a different angle on the filters in front of the detectors.

Table 3-2 *Values and uncertainties for photon counts (earlier set)*

	Value	Uncertainty (absolute)
N_C	1886457	1593
N_{acc}	27256	120
N_{trig}	10000000	0
N_{false}	206852	561
QE[1]	0.190	0.0016

Table 3-3 *Values and uncertainties for photon counts (later set)*

	Value	Uncertainty (absolute)
N_C	1895768	1219
N_{acc}	16874	376
N_{trig}	10000000	0
N_{false}	206852	561
QE[1]	0.192	0.0013

The angle of incidence on a filter is important for three reasons. Firstly, refraction through the filter will displace the transmitted light, leading to the PDC being imaged on a different region of the detector active area. Secondly, at different angles, the spectral transmittance of the filters is changed (see Figure 3-7), which may mean that we are be registering photons at a different wavelength. If the effective transmittance curve of the trigger filter is shifted in one direction, then we need to ensure that the

[1] Intermediate result without correcting for the transmittance.

transmittance of the DUT filter covers the conjugate wavelength, which will be shifted in the opposite direction. Lastly, the QE is a function of wavelength, so as a consequence of the change in spectral transmittance, the measured spectral profile will be correspondingly distorted.

To check the angles of incidence, a HeNe laser is set up and reflected through the crystal on to the filters and the displacement of the reflections measured. It was found, after the later measurements, that there was an angle of incidence of 3.2º on the trigger filter and 2.4º on the DUT. In future experiments this problem should try to be rectified. This may involve rotating the crystal (or using a new crystal, cut differently) since, as illustrated in Figure 2-5 and Figure 2-6, as the pump makes a smaller angle with the optic axis, the chromatic dispersion increases, making it easier to resolve a particular wavelength.

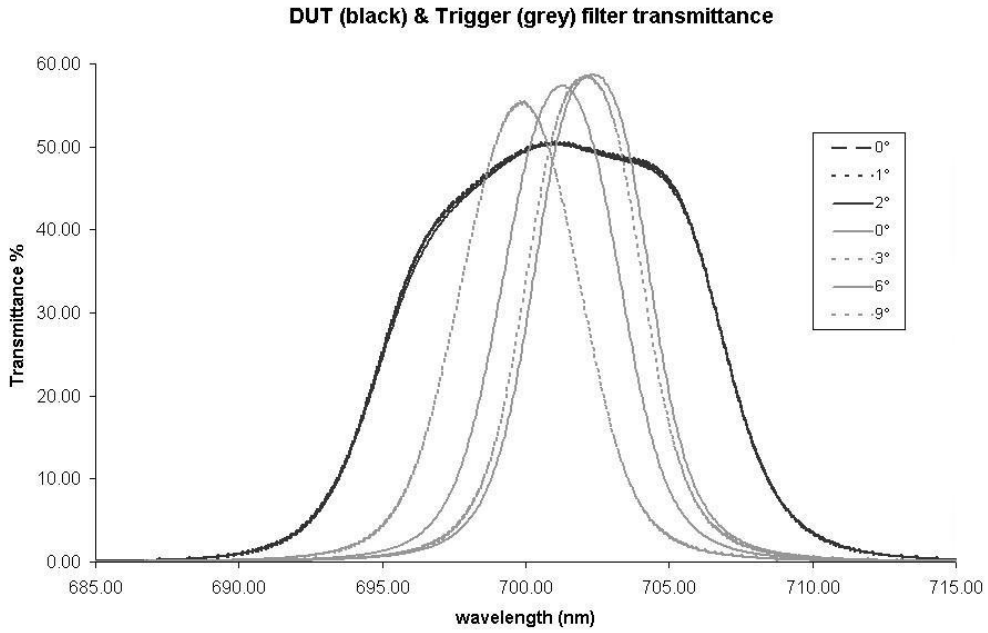

Figure 3-7 *Transmittance measurements of the filters used in front of the DUT and trigger at different angles of incidence [by N.Walker, NPL]. Note the shift towards the left of the transmittance peak for the trigger filter as the angle of incidence is increased.*

The largest relative uncertainty in photon counts is due to the coincidence and accidental counts. This can be improved by increasing the number of triggers counted as noted before in section 3.2.1.

3.6.2 Correcting for the transmission of the DUT channel

In section 3.2.2, the validity of approximating the transmittance from the centre of the crystal to the square root of the total transmittance was discussed. Calculations [xvii] based on this approximation give the transmittance of the downconverted light as 0.983 ± 0.005. This incorporates a factor accounting for the angle of the emitted light. The fractional uncertainty in this figure is 0.5%, as compared with the average fractional uncertainty of 0.08% found in the photon number measurements above. Clearly, the transmittance through the crystal contributes the greatest uncertainty at this point.

Since, in practice, a detector will be used in conjunction with a filter and lens, we can treat all the optical elements in the DUT path as a single system and find the QE for this. Using the value for the transmittance given above together with the average of the results found in the last section, i.e. 0.191 for the total QE we have 0.194 ± 0.001 which corresponds to a fractional uncertainty of 0.5%. Taking account of the filters, a QE of the order 0.38 is found, which appears to be in line with the specifications in Appendix E.

4. Spectral radiance

4.1 Spectral radiance in terms of fundamental constants

We saw in section 2.2 that the quantum mechanical analysis of PDC predicted spontaneous downconversion, which was interpreted as being stimulated by one photon per mode background fluctuations. We now consider a source of signal photons incident on a pumped medium such that the phase matching conditions are met. We will now have parametric amplification of the signal, together with a correlated growth in the idler fields (see Figure 4-1). Assuming that there is no initial input at the idler frequency, then from (2.16) we have, with the signal on,

$$\langle N_i(t)\rangle_{ON} = (1 + \langle N_{s0}\rangle)\sinh^2\kappa \tag{4.1}$$

With the signal off, $\langle N_{s0}\rangle = 0$, so taking the ratio of $\langle N_i(t)\rangle_{ON}$ and $\langle N_i(t)\rangle_{OFF}$ and rearranging, we have

$$\frac{\langle N_i(t)\rangle_{ON}}{\langle N_i(t)\rangle_{OFF}} - 1 = \langle N_{s0}\rangle \tag{4.2}$$

Although this equation is dimensionless, numerically $\langle N_{s0}\rangle$ is the average number of photons per mode of the initial signal field. Now a spectral radiance of one photon per mode can be written [vi]

$$R_{vac} = \frac{\eta c^2}{\lambda} \tag{4.3}$$

Thus, by counting the photons in the idler field, we can make an absolute measurement of the signal spectral radiance in terms of the fundamental constants *h* (Planck's constant) and *c*, the speed of light. A spin-off from this technique is that, where the signal may be in the infrared, we can arrange the idler photons to be in the visible range, where detection technology is better.

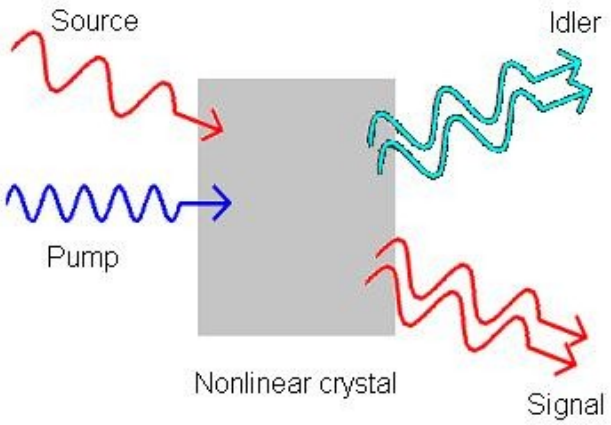

Figure 4-1 *Schematic of parametric amplification due to stimulated parametric downconversion in a nonlinear crystal.(Adapted from [xvi]).*

In practice, (4.2) needs to be modified to take account of transmission losses, the transfer function of the imaging optics and how well the source is overlapped with the pump in the crystal. Subsuming all these factors into a single term *T*, (4.2) becomes

$$\frac{1}{T}\left[\frac{\langle N_i \rangle_{ON}}{\langle N_i \rangle_{OFF}} - \right] = \langle N_{s0} \rangle \qquad (4.4)$$

These factors are discussed in section 4.4.

4.2 Experimental set up

The proposed scheme will employ Type II collinear downconversion, using a copper point blackbody (CuBB) as the source to be measured. A schematic of the experimental set up is shown in Figure 4-2. The source radiation is to be collimated and will enter the BBO crystal collinearly with the pump beam. A filter selects out the visible photons correlated with the stimulated radiation and an aperture ensures that it is only the collinear downconverted light the detector receives. A shutter is used to switch off the source so that the spontaneous downconversion can be measured. The half-wave plates are used to achieve the correct polarisation for the PDC.

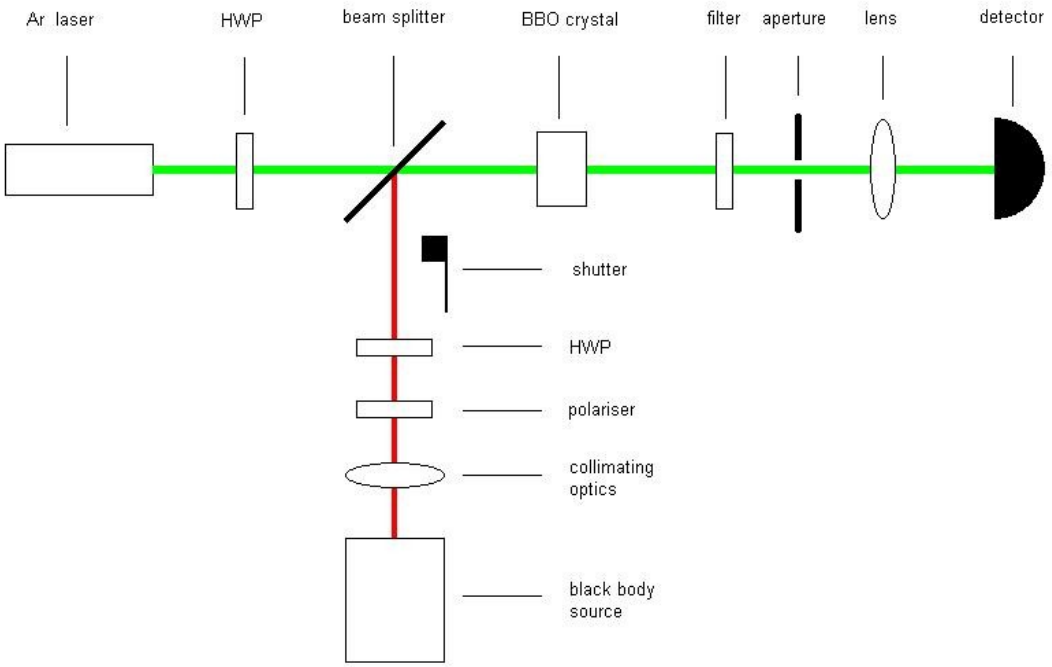

Figure 4-2 *Schematic of spectral radiance measurement set up using Type II collinear downconversion*

The CuBB operates by melting very pure copper surrounding the cavity itself (see Figure 4-3) and then cooling it below its freezing temperature. Due to the purity of the copper, it will under-cool without freezing as there are few seed sites to initialise the

crystallisation. As it does freeze, the temperature rises back up to the freezing point temperature (1.358×10^3 K) where it remains stable for some time. By Wien's Law, the maximum emission at this temperature is at 2.134 μm.

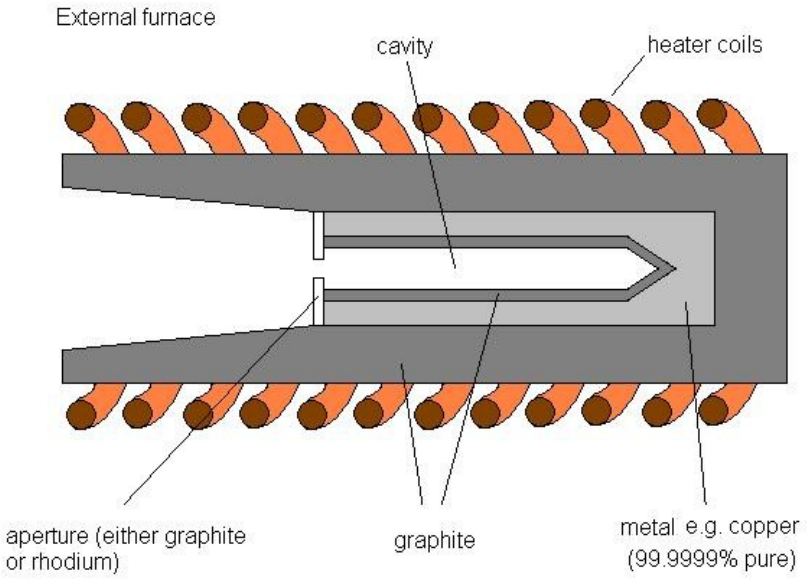

Figure 4-3 *Generalised schematic of a fixed-point blackbody. The blackbody radiation is emitted from the central cavity, held at a constant temperature by the freezing of the very pure metal surrounding it. (Based on a sketch by E. Woolliams).*

In order to image the blackbody cavity and collimate the beam, we propose to use an off-axis parabolic mirror (OAPM). This is a section taken from a parent parabolic mirror that enables light from a point source to be collected, collimated and turned by a fixed angle. Figure 4-4 shows a schematic of an OAPM indicating the meaning of the terms 'real' and 'apparent' focal length.

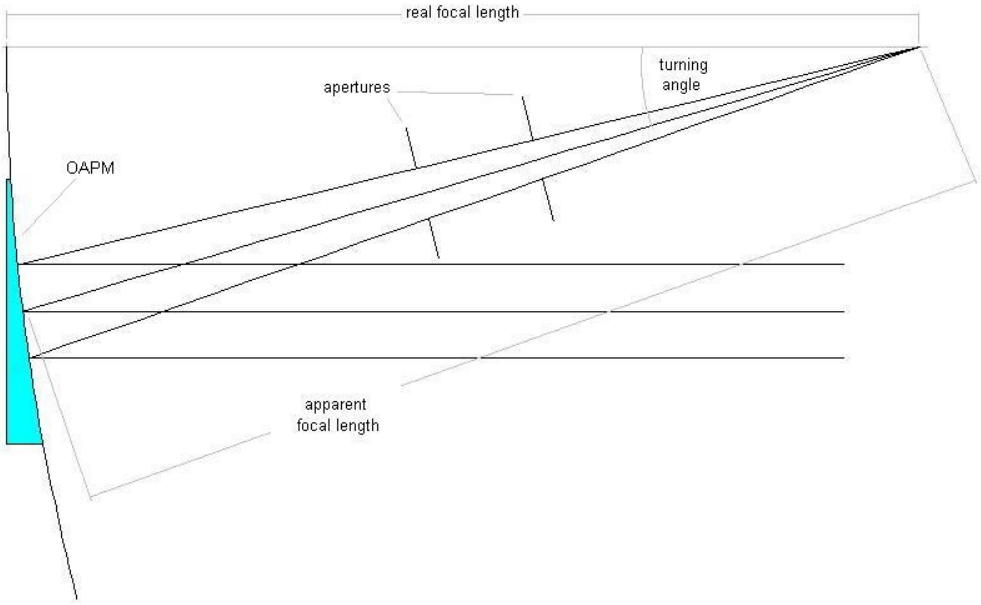

Figure 4-4 *Schematic of an off-axis parabolic mirror. The shaded region represents the mirror sectioned from the parent (the parabolic curve shown).*

Since the distance from the outside aperture to a point in the cavity in the CuBB is about 400 mm, the apparent focal length needs to be greater than this. The size of the CuBB also means that, in order to make room for it in the laboratory, it would be practical to have it lying alongside the optical bench and use a 90º turn on the OAPM. Unfortunately, off-the-shelf OAPMs with this apparent focal length and turning angle are not available. This is because the parent parabolic mirror would have to be exceptionally large. Instead, such a mirror would have to be fabricated as a 'stand alone' mirror. Since high quality off the shelf mirrors cost thousands of dollars, this is likely to be a very expensive option.

Another consideration must be the coating on the mirror. For short wavelengths, aluminium may be sufficient but longer than 2 microns, we would have to use gold

coatings. The choice of wavelength may therefore affect our mirror specifications. Naturally, we would also need to characterise the transfer function of the mirror.

4.3 Downconversion options

For the spectral radiance measurements, we had a second BBO crystal available, cut with the optic axis at 49.2º to the normal and rotated by an azimuthal angle of 30º (as marked by the suppliers) for Type II downconversion. This implies that the suppliers are using the alternative crystal orientation to that used in deriving (2.31). That is, the effective nonlinearity is given by

$$d_{eff} = l_{11} \cos^2 \theta_{\cdot} \sin 3\phi_{\cdot,} \qquad \text{(Type II)} \tag{4.5}$$

using the suppliers' convention for ϕ (see section 2.4).

The argon ion laser can be tuned to several different wavelengths, so different options for downconversion are available. Table 4-1 lists the results for Type II collinear downconversion, using three different sources for the Sellmeier indices (Photox is the company that supplied our first crystal). The values shown are for normal incidence.

A potential problem is the discrepancy in the results – up to 5 nm for the e wave and 60 nm for the o wave. Figure 4-5 shows the calculations for the lab angles of the emergent downconverted light cones with a pump at 514.5 nm (using Ghosh as in Appendix A). The first figure shows the collinear case (the smaller cone corresponds to the e wave), whilst the second shows what happens when the e wave is changed in

wavelength by 5 nm. It may therefore be necessary to determine the wavelengths of the downconverted light in the collinear case for our crystal experimentally.

Table 4-1 *Wavelength options for Type II collinear downconversion (normal incidence).*

Reference	pump (μm)	(e) wave (μm)	(o) wave (μm)
(Ghosh)	0.5145	0.6654	2.2691
	0.4880	0.6408	2.0461
	0.4579	0.6215	1.7393
	0.3511	0.6994	0.7051
(Kwiat)	0.5145	0.6674	2.2452
	0.4880	0.6431	2.0238
	0.4579	0.6234	1.7246
	0.3511	0.6957	0.7088
(Photox)	0.5145	0.6623	2.3061
	0.4880	0.6390	2.0654
	0.4579	0.6212	1.7421
	0.3511	0.7023	0.7021

Alternatively, we can choose a wavelength and try to find the phase-matching angle to achieve it. 800 nm would be a convenient choice, attainable with a pump at 351.1 nm (Table 4-2), since a filter radiometer (see [ii]) is available at this wavelength for monitoring the blackbody. This would allow direct comparisons of the correlated photons method to be made to a conventional technique. Achieving these angles with the current crystal would necessitate rotating it.

Table 4-2 *Calculation of phase-matching angle to achieve 800nm downconversion using a pump at 351.1 nm*

Reference	(e) wave (μm)	(o) wave (μm)	theta (degs)
(Ghosh)	0.6257	0.8000	52.99
	0.8000	0.6257	45.30
(Kwiat)	0.6257	0.8000	52.86
	0.8000	0.6257	45.11
(Photox)	0.6257	0.8000	53.08
	0.8000	0.6257	45.46

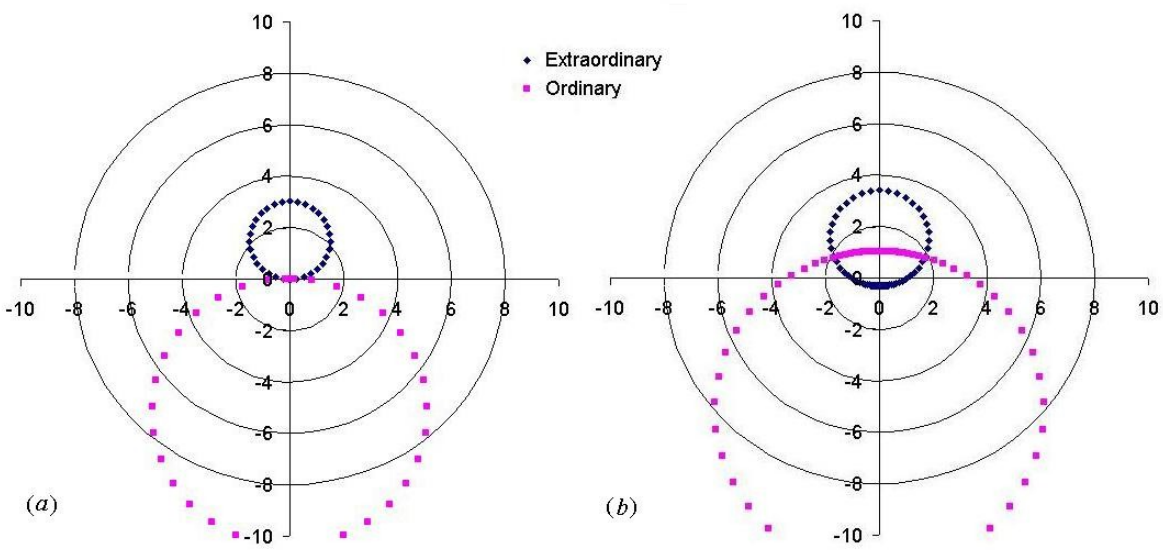

Figure 4-5 *Laboratory angles (relative to the pump beam) for Type II downconversion with a pump of 514.5 nm. (a) e wave = 665.4 nm. (b) e wave = 670 nm. The dots indicate the light cones seen on exit. The smaller cones correspond to the e waves. From this direction, the optic axis would be projected along the vertical line, which would therefore be rotated by the azimuthal angle in the lab.*

4.4 Sources of uncertainty

4.4.1 Pump stability

A first point to note is that in deriving (4.2) from (4.1) we assumed that the $\sinh^2 \kappa t$ term would cancel for the number densities with the signal on and off. However,

comparing κ to the analogous gain term g in (2.10) for the classical analysis, we see that there is a dependence on the pump intensity. Any fluctuations in the pump between runs would therefore introduce uncertainties in the downconverted number densities. In practice, this can be overcome using a stabilised laser and making these measurements close together so that alignment conditions do not change. Also, since the number densities in (4.2) are averages, we should take measurements over fairly long counts so that the fractional uncertainties are reduced. This should also help to average out any instability in the pump.

4.4.2 Detector linearity

Since (4.2) involves a ratio of the idler number densities, the absolute values are not significant. This implies that the detector used does not actually need to be calibrated; the only requirement is that it gives a linear response over the range of photon counts. In practice, this may be an issue, since photon detectors and the counting electronics have a dead time during which they cannot register a second photon. At high photon arrival rates, counts may be lost, so the linearity of the photon counting modules must be characterised.

4.4.3 Transfer function of optics

In order to image the radiant source and collimate it onto the nonlinear crystal, we need some kind of imaging optics. In section 4.2 we proposed using an off-axis parabolic mirror. In order to test the method, we envisage using a black body source since this is a standard reference. For the technique to be generally applicable to spectral radiance measurement, we would want to measure an arbitrary source. Therefore we need to calculate the transfer function of the imaging optics so that we

can extrapolate back from any results to the original source and ascertain how accurately this can be done.

4.4.4 Overlap factor and transmission losses

As in the QE measurements, we also need to take the transmission losses in the crystal and any other optics into account. Depending on the experimental set up, analysing the transmission of downconverted light may be more complicated than for the QE measurements. In the latter case, we assumed that downconversion takes place equally throughout the thickness of the crystal, so we could take the centre as the average point. This remains a valid assumption for spontaneous PDC but for stimulated PDC it will depend on how well the signal overlaps the pump and the downconverted modes.

This overlap factor will involve three components. Firstly, how well the source overlaps spatially with the pump. This will determine the rate of any downconversion. Secondly, the signal must overlap spectrally with the downconverted light in order to achieve parametric amplification at the required frequencies. Thirdly, the source must overlap angularly with the downconverted light. These last two points are of course related and correspond to the phase matching requirements.

The first of these components has been calculated by Migdall *et al* [vi] at NIST by taking the integral of the product of the source and pump profiles and normalising this to the pump. In the NIST experiments, this was complicated by the fact that they were using non-collinear downconversion. It is hoped that in our proposed experimental set up, using collinear downconversion and encompassing the pump entirely by

collimated source radiation will simplify the analysis. How accurately this can be done will depend on the profile we can get for the collimated source.

The second aspect should be fulfilled automatically for a particular pair of wavelengths in the collinear case. The question will be how accurately we can know what those wavelengths are. This will involve how the crystal is cut, how it is rotated and what filters are used. Also, predicting these wavelengths can be difficult due to the discrepancy in sources for the Sellmeier indices for BBO, discussed in section 4.3. Again, the collinear arrangement with the collimated source should simplify the analysis for the angular overlap. The uncertainties here will arise in how well we can align the optics to achieve this.

Having considered how well the source and pump overlap spatially, angularly and spectrally, we can consider where the mean point of downconversion will be, necessary for establishing the transmittance of the crystal. For our arrangement, this should again be the centre of the crystal. The problem that emerges is then considering reflections at the boundaries. Rotating the crystal will change the spectral transmittance of any AR coating on the exit face. Also, we may wish to use the same crystal at different frequencies. This means that approximations used in section 3.6.2 may no longer be valid and further analysis may be required.

5. Discussion and conclusions

The current research in quantum metrology using correlated photons offers a new approach to the determination of radiometric scales in the photon counting regime. Whereas these scales are currently based on calibrated detectors, via cryogenic radiometry and known sources (such as blackbodies or synchrotron radiation), the use of correlated photons offers a technique to determine detector and source scales directly and absolutely. If this technique is to compete with cryogenic radiometry as a method of realising primary radiometric scales, then improvements in accuracy of one or two orders of magnitude are necessary. Improvements by a factor of ten or less may still make this a viable technique for measurements in the photon counting regime.

For the quantum efficiency measurements, the largest current uncertainty is associated with the transmission through the crystal. The data from Table 3-1 for transmittance, absorption and scattering, suggests that realisable uncertainties for the loss in the crystal could be as low as 0.02% (as compared to 0.5% used in section 3.6.2). However, this neglects the uniformity and stability of the crystal, which may vary by a greater extent than this. It may need to be established whether the local heating of the crystal causes transient changes in the transmission or permanent optical damage. The temperature dependence of the refractive indices also needs to be quantified. Given any spatial changes in uniformity, another issue would be wandering of the pump beam, so this should be quantified.

A further complication arises through the use of AR coatings. Generally, the crystal will have an AR coating at the downconverted wavelengths on the output face and a

coating at the pump wavelength on the input side. This lack of symmetry limits how accurately the transmittance from the centre of the crystal can be modelled by the square root of the total transmittance. With detailed information about the thin films used (i.e. number, thickness and refractive indices of the layers), it may be possible to derive more accurate theoretical predictions using Fresnel's equations. Alternatively, the reflectivities at the wavelengths of interest might be determined empirically. In all cases, a robust experimental set up is necessary to establish the required uncertainties in the losses and ensure reproducibility.

Quantifying the uncertainties associated with the alignment is difficult in practice. The proof of the alignment and alignment procedures lies in the reproducibility of the measurements. It was noted in section 3.6.1 that after the stages had been aligned to obtain maximum counts, the filters were not normal to the crystal. As mentioned in that section, this can introduce uncertainties due to change in the way that the detector active areas are irradiated and shifts in spectral selectivity. This may necessitate changes in the alignment procedure.

At present, the filters are fixed to the front plates with double sided tape. Since these plates may not be perfectly normal to the base plates on which the lens / detector assemblies are mounted, it may be to mount the filters in adjustable holders so that they can be adjusted for normality at the start of the alignment procedure. After the initial round of alignment scans, the filters could be checked for normality to the crystal as described in section 3.6.1. The stages could then be rotated until the filters were contra reflecting and the optimisation repeated.

Also, the angle of the optic axis with pump beam can be reduced, either by rotating the crystal or using another cut differently. At smaller angles there is higher chromatic dispersion, i.e. the rate of change of cone angle with wavelength is greater. This allows a given wavelength to be resolved more accurately.

The uncertainties associated with photon counting are much smaller than the transmittance uncertainties. As improvements in transmission measurement are made, these may need to be reviewed. If the photon arrival times are assumed to be Poisson distributed, then the uncertainties can be taken as the standard deviation, i.e. the square root of the mean. In this case the relative uncertainties should decrease as one over the square root of the number of counts. However, it was found that the measured standard deviations differed from the square roots of the averaged photon counts. It was suggested that this may be due variation in the pump intensity. Bearing in mind that the laser is light stabilised to give a constant optical output power, it is possible that fluctuations are arising in intermediate optical elements (as was found in the transmittance measurements reported in section 3.5, where the introduction of the HWP introduced significant noise into the measurements). Even if this is the case, the effect of taking counts for longer should average these fluctuations out and reduce the relative uncertainties. In principle, it should be possible to choose a number of counts to take that will make these uncertainties arbitrarily small. The actual standard deviations can be found empirically, thereby establishing what number of counts will be necessary.

The counting electronics is another area that requires investigation. The problems with reflections due to impedance mismatching were discussed in section 3.3. The

reflections themselves did not cause particular problems since they were not overlapping with the coincidence peak and could be safely excluded from the integration of the counts. An interesting feature that, as yet, has not been explained is the increase in the background level after the first reflection (see Figure 3-6 *a*). Supposedly, if all the counts were being reflected, there should be the same level of noise before the reflection as there is after. It is not obvious that this will affect the accuracy of the measurements but this should be investigated. Given that the 9308 counter is designed to take NIM pulses as input and that the pulses used were in fact attenuated and inverted TTL pulses, it would not be surprising if the performance of the electronics was compromised. It is hoped that the arrival of the bespoke TTL-NIM converter will improve the reliability of the counting system.

Many of the points discussed above will also be applicable to the spectral radiance measurements once the experiment is set up. Particular details relevant to this method have already been discussed in section 4.4. As with the QE measurements, good alignment and a robust experimental set up will also be crucial. In addition to the alignment of the laser optics and maximising counts on the detector (where a similar procedure to that discussed previously may be used), there is also the alignment of the off-axis parabolic mirror to be considered. Possibly, this might also be mounted on automated stages. An alignment procedure may then be to optimise the detector for spontaneous PDC and then optimise the mirror alignment for stimulated PDC.

At present, the main focus of work for improving these techniques with correlated photons lies in realising better uncertainties for transmission losses in the crystal, ensuring good alignment of the experimental apparatus and developing effective

procedures for achieving this. Using current techniques for transmittance measurements, there seems to be no reason in principle why improvements of an order in magnitude might not be achieved. In order that these uncertainties should be on a par with those currently realised in cryogenic radiometry, further improvements would be needed.

6. Acknowledgements

The author would like to acknowledge the following for their help and participation in this work: Dr Chris Chunnilall, project supervisor; Dr Jessica Cheung, co-worker and co-author of the software; John Mountford for writing the TP stage drivers as well as advice and assistance with the electronic equipment; Emma Woolliams for general advice on metrology and Dr Leon Rogers for facilitating the student placement at NPL.

7. Appendices

A. Sellmeier equations for BBO

The refractive indices for BBO used in this report are calculated using the following Sellmeier equation due to [20] where the Sellmeier constants are given in the table below.

$$n = \left(A + \frac{B}{1 - C/\lambda} + \frac{D}{1 - E/\lambda} \right)^{1} \tag{A.1}$$

Table A-1 *Sellmeier constants for BBO*

	o-ray	**e-ray**
A	1.7018379	1.5920433
B	1.0357554	0.7816893
C	0.018003440	0.016067891
D	1.2479989	0.8403893
E	91	91

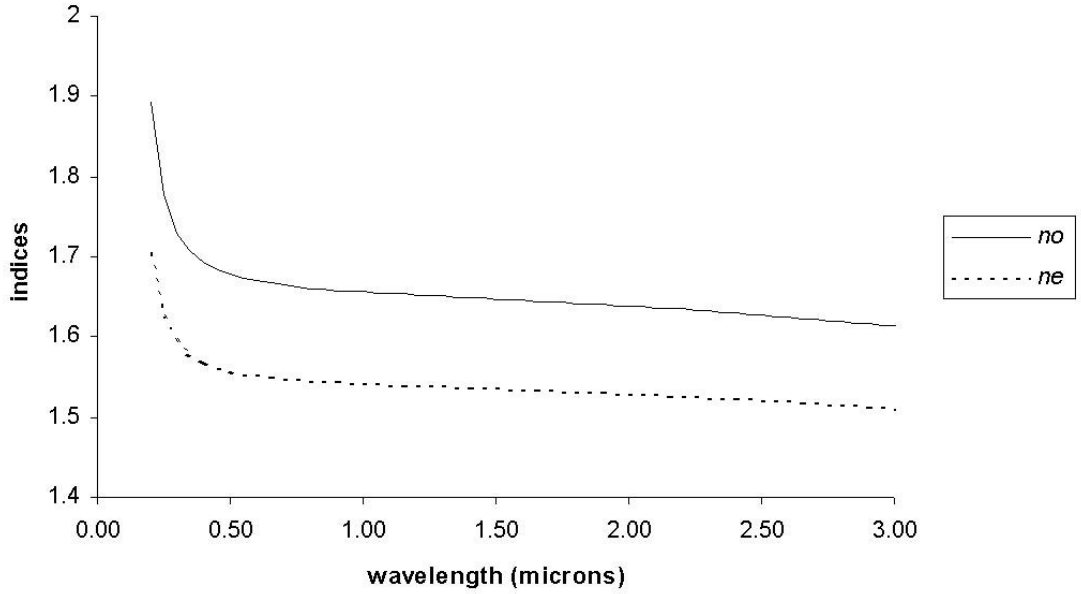

Figure A-1 *Refractive indices for BBO*

B. Visual Basic functions for phase matching calculations

The Visual Basic functions for Type II phase matching, used in Excel are listed here. Functions for Type I downconversion were also written though these are fairly trivial and are not listed. For clarity of reading, comments are type set in italic and Visual Basic keywords in bold. In order to use these functions, the inverse trigonometric functions arccos and arcsin were also be defined as only arctan is defined in the version of Visual Basic used.

```
' Sellmeier indices
Const A_e As Double = 1.5920433     'extraordinary
Const B_e As Double = 0.7816893
Const C_e As Double = 0.016067891
Const D_e As Double = 0.8403893
Const E_e As Double = 91
Const A_o As Double = 1.7018379     'ordinary
Const B_o As Double = 1.0357554
Const C_o As Double = 0.01800344
Const D_o As Double = 1.2479989
Const E_o As Double = 91
' Speed of light (microns per sec)
Const C As Double = 299000000000000#
Const pi As Double = 3.14159265358979


Public Function NE(L As Double) As Double

' calculates the extraordinary refractive index of BBO as a function of
wavelength
' (i.e. half the extraordinary axis of the index ellipsoid)

'Arguments :
'   L = wavelength (in microns)

NE = Sqr(A_e + B_e / (1 - C_e / (L * L)) + D_e / (1 - E_e / (L * L))) 'Ghosh

End Function


Public Function NO(L As Double) As Double

' calculates the ordinary refractive index of BBO as a function of
wavelength

' Arguments :
'   L = wavelength (in microns)


NO = Sqr(A_o + B_o / (1 - C_o / (L * L)) + D_o / (1 - E_o / (L * L))) 'Ghosh

End Function
```

```
Public Function Ntheta(L As Double, t As Double) As Double

' calculates the extraordinary refractive index of BBO at a given wavelength
as a function
' of angle from the optic axis


' Arguments :
'   L = wavelength (in microns)
'   t = angle from optic axis

If Cos(t) = 0 Then  't = pi/2 + n*pi
    Ntheta = NO(L)
    Exit Function
Else
   Ntheta = NE(L) * NO(L) * Sqr((1 + Tan(t) * Tan(t)) / (NE(L) * NE(L) +
NO(L) * NO(L) * Tan(t) * Tan(t)))
End If

End Function


Public Function FindTheta1(thetaPM As Double, wp As Double, w1 As Double,
phi1 As Double) As Double

' calculates the angle of the k1 wavevector to kp
' Uses the Newton-Raphson method, where the derivative of the function dk
(the phase mismatch we want equal to zero)
' is approximated by a central difference

' Arguments:
'   thetaPM = the angle of the pump from the optic axis
'   wp = the pump angular frequency
'   w1 = the angular frequency of k1
'   phi1 = the azimuthal angle of k1 around the pump beam


Dim iter As Integer
Dim w2 As Double, theta As Double, theta1 As Double, theta2 As Double
Dim kp As Double, k2 As Double, k1_1 As Double, k1_2 As Double, k1 As
Double, L1 As Double
Dim alpha1 As Double, alpha2 As Double, alpha As Double
Dim dk1 As Double, dk2 As Double, dk As Double

w2 = wp - w1
theta = pi / 2 ' try to find +ve solution for theta
dt = 0.00001

kp = Ntheta(2 * pi * C / wp, thetaPM) * wp / C
k2 = NO(2 * pi * C / w2) * w2 / C
L1 = 2 * pi * C / w1 ' wavelength of k1


For iter = 1 To 20

    theta2 = theta + dt
    theta1 = theta - dt
    alpha = arccos(Cos(thetaPM) * Cos(theta) + Sin(thetaPM) * Sin(theta) *
Cos(phi1))
    alpha1 = arccos(Cos(thetaPM) * Cos(theta1) + Sin(thetaPM) * Sin(theta1)
* Cos(phi1))
    alpha2 = arccos(Cos(thetaPM) * Cos(theta2) + Sin(thetaPM) * Sin(theta2)
* Cos(phi1))
```

```
    k1 = Ntheta(L1, alpha) * w1 / C
    k1_1 = Ntheta(L1, alpha1) * w1 / C
    k1_2 = Ntheta(L1, alpha2) * w1 / C
    dk = kp * kp - k2 * k2 - 2 * kp * k1 * Cos(theta1) + k1 * k1
    dk1 = kp * kp - k2 * k2 - 2 * kp * k1_1 * Cos(theta1) + k1_1 * k1_1
    dk2 = kp * kp - k2 * k2 - 2 * kp * k1_2 * Cos(theta2) + k1_2 * k1_2

    theta = theta - 2 * dk * dt / (dk2 - dk1)

Next iter

FindTheta1 = theta

End Function


Public Function FindTheta2(thetaPM As Double, wp As Double, w1 As Double,
phi1 As Double, theta1 As Double) As Double

' calculates the angle of the k2 wavevector to kp

' Arguments:
'   thetaPM = the angle of the pump from the optic axis
'   wp = the pump angular frequency
'   w1 = the angular frequency of k1
'   phi1 = the azimuthal angle of k1 around the pump beam
'   theta1 = the angle of k1 to the pump beam

Dim w2 As Double
Dim k2 As Double, k1 As Double
Dim alpha As Double

w2 = wp - w1
alpha = arccos(Cos(thetaPM) * Cos(theta1) + Sin(thetaPM) * Sin(theta1) *
Cos(phi1))
k1 = Ntheta(2 * pi * C / w1, alpha) * w1 / C
k2 = NO(2 * pi * C / w2) * w2 / C

FindTheta2 = arcsin(-k1 * Sin(theta1) / k2)

End Function


Public Function FindLab1(thetaPM As Double, theta As Double, phi1 As Double,
w1 As Double) As Double

' calculates the laboratory angle (via Snell's) law for the k1 vector

' Arguments:
'   thetaPM = the angle of the pump from the optic axis
'   theta = the angle of k1 to the pump beam (inside the crystal)
'   phi1 = the azimuthal angle of k1 around the pump beam
'   w1 = the angular frequency of k1


Dim alpha As Double, n1 As Double

alpha = arccos(Cos(thetaPM) * Cos(theta) + Sin(thetaPM) * Sin(theta) *
Cos(phi1))
n1 = Ntheta(2 * pi * C / w1, alpha)

FindLab1 = arcsin(n1 * Sin(theta))

End Function
```

```
Public Function FindLab2(theta As Double, w2 As Double)

' calculates the laboratory angle (via Snell's) law for the k2 vector

' Arguments:
'   theta = the angle of k2 to the pump beam (inside the crystal)
'   w2 = the angular frequency of k2

Dim n2 As Double

n2 = NO(2 * pi * C / w2)

FindLab2 = arcsin(n2 * Sin(theta))

End Function


Public Function arccos(x As Double) As Double

' calculates the inverse cosine

' Arguments:
'   x = cosine

arccos = Atn(Sqr(1 - x * x) / x)

End Function


Public Function arcsin(x As Double) As Double

' calculates the inverse sine

' Arguments:
'   x = sine

arcsin = Atn(x / Sqr(1 - x * x))

End Function
```

C. LabView Software User Manual

LabView is a graphical programming language used to read and control equipment using a PC via some communications protocol, typically RS232-C (serial port) or GPIB. Modules written in LabView are called 'virtual instruments' or 'VIs'. The structure of a program becomes hierarchical as 'sub-VIs' are incorporated into other VIs. Sections of code are often described as 'wiring diagrams'.

In our experiments, our requirements were the control of the stages to position the detectors and reading the counter electronics. Ultimately, the VIs will be compiled into an executable for the correlated photons project. Due to its graphical nature and much of the code being hidden in multiple case structures, sequence structures and sub-VIs, it is not practical to print out the source code. Instead, this appendix is intended as a user manual to the stage control and counter reading software.

Moving the TP stages and reading the 994 counter

After starting the application, select 'move TP stages' from the 'mode' drop-down menu. This opens the TP stage control window (Figure C-1). Select the stage to be moved from the drop-down box. Note that *X* is the horizontal axis and *Y* is the vertical. Enter the distance to be moved in the 'MOVE' box and either press 'Enter' or click on the 'MOVE' button. Depending on whether the stage is translation or rotation, the units will be either mm or degrees. The position of the stage is then updated in the corresponding text box below. If the stages need to be stopped immediately, click on 'KILL'.

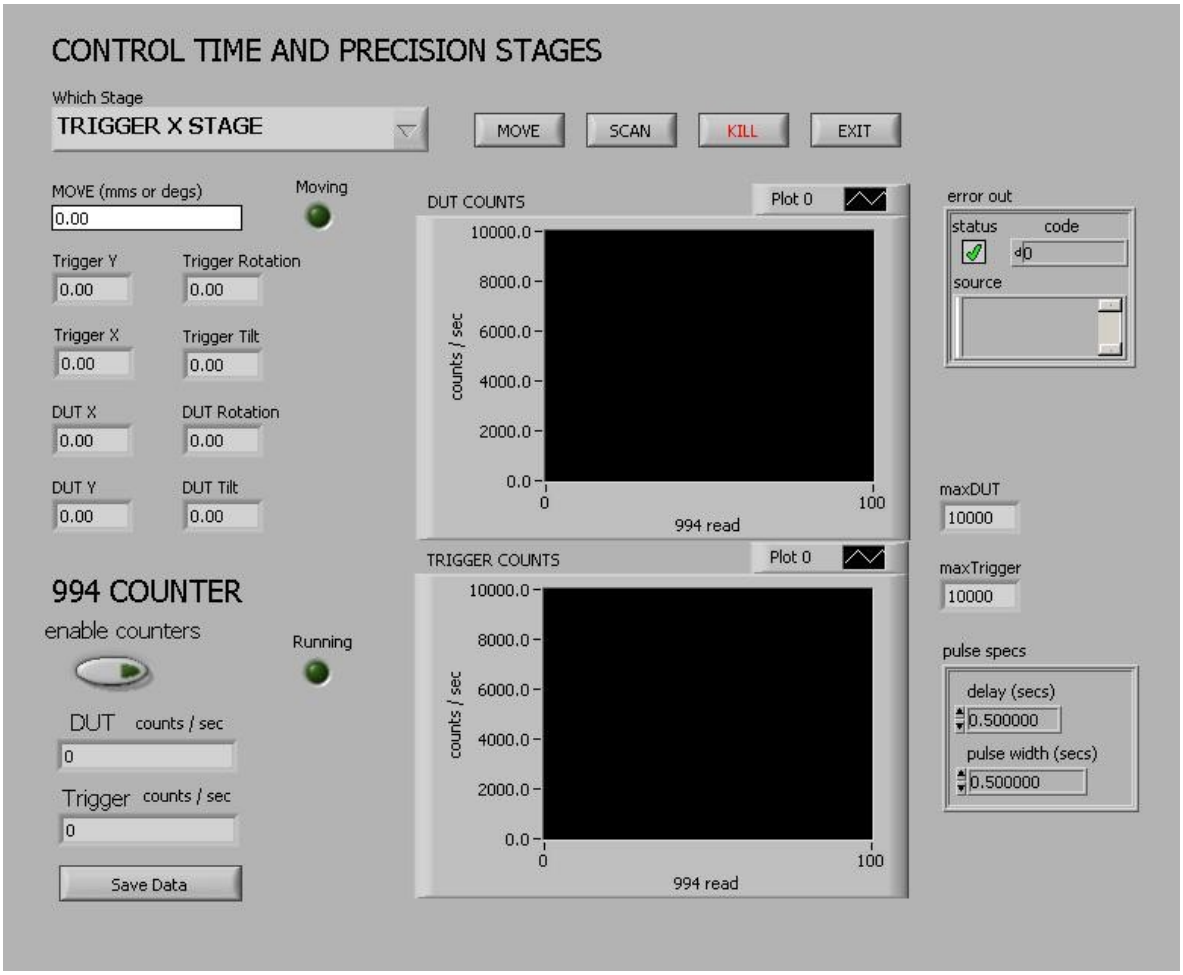

Figure C-1 *Window for controlling the TP stages and reading the 994 counter.*

If a 994 count is required at the end of the move, the ‘enable counters’ button must be toggled to ‘on’, when it ‘lights up’. The individual counts are returned in the boxes below this, whilst a record of the counts for each detector is plotted on the charts. To take a count without moving, just enter zero in the ‘Move’ box. Clicking on ‘Save Data’ saves this data in a spreadsheet file, with the trigger counts in the first column and the DUT counts in the second.

The ‘pulse specs’ box on the right hand side of the window sets the parameters for the 994 counter VI. The counts are divided by the pulse width to give the counts per second.

Clicking on ‘EXIT’ closes the VI and takes you back to the main window.

Scanning over an axis

To scan over an axis, select the required axis in the ‘Which Stage’ box and click on the ‘SCAN’ button. This opens the window shown in Figure C-2.

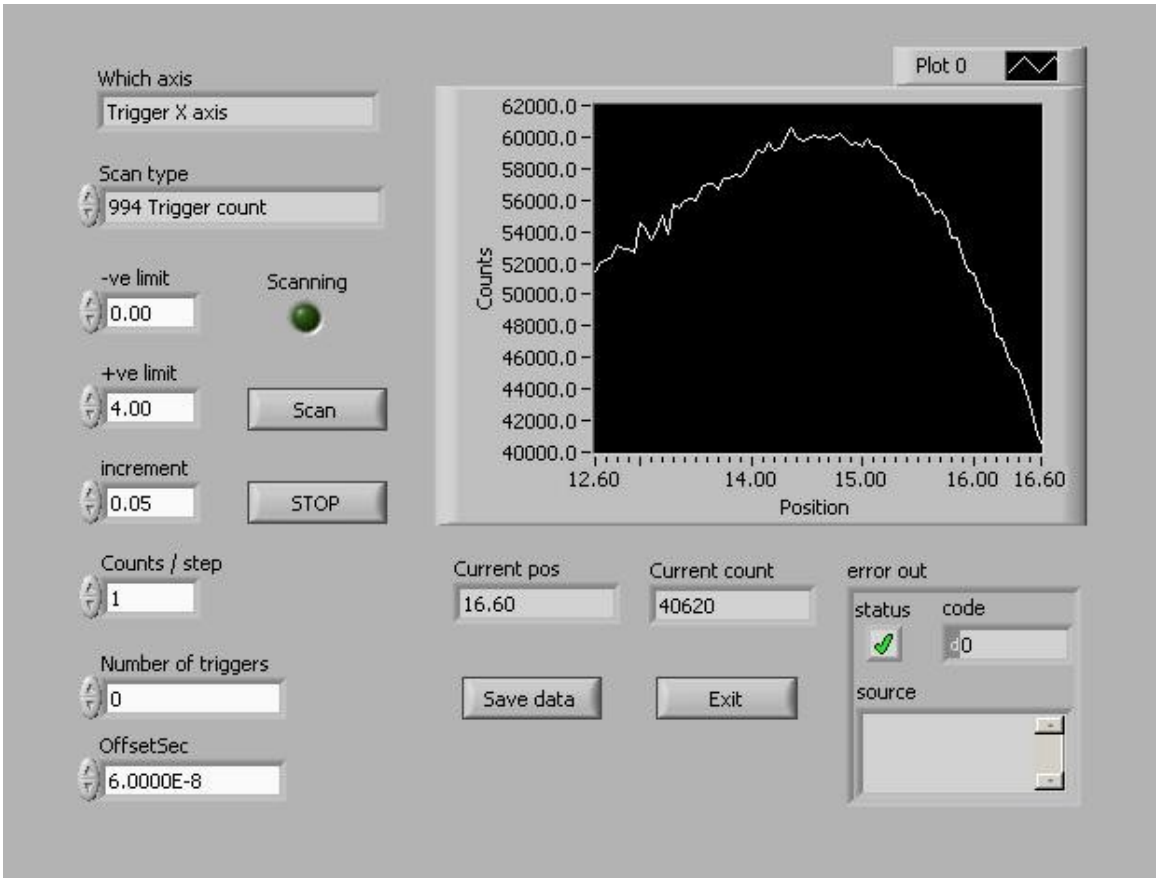

Figure C-2 *The Scan-Axis window*

The scans can either read from the 994 counter (either the Trigger or the DUT) or the 9308 counter. Ensure that these counters are connected to the detectors correctly before continuing. The –ve and +ve limit boxes give the limits of the scan around the position started in when the VI was called. E.g., if you are currently at 2mm on the *X* axis and enter 5 mm for both limits, then the scan will be from –3 mm to 7 mm. (Note, if scanning a rotation axis, these units become degrees).

The ‘Counts / step’ box specifies how many counts (which are then averaged) will be performed each time the stage stops. A high count reduces the noise but increases the time for a scan to be performed.

The ‘Number of triggers’ and ‘OffsetSec’ boxes are only used in conjunction with a 9308 scan. For a relatively fast scan with reasonable noise, 50000 triggers is advised. The ‘OffsetSec’ is the time the 9308 waits after being triggered before it starts counting. The counting span is set at 80 ns and is not configurable from this window.

To start the scan, click on ‘Scan’. If the scan needs to be interrupted, click on ‘STOP’. Note that it may be a few seconds before this takes effect. Figure C-2 shows a typical scan. ‘Save data’ saves this as a spreadsheet file with the name of the axis with the position and counts in two columns.

Whilst the window is open, further scans are always relative to the initial start position. However, after completing a scan, the stage is not returned to its start point. Clicking on ‘Exit’ returns you to the move TP stages window and the new position is updated in the relevant text box.

Counting coincidences

To perform coincidence counts with the 9308 once the detectors are aligned, return to the main window and select ‘COINCIDENCES, from the ‘Mode’ menu. This opens the window shown in Figure C-3. If the ‘Connected’ light does not come on, check that the USB cable from the 9308 is connected to the PC.

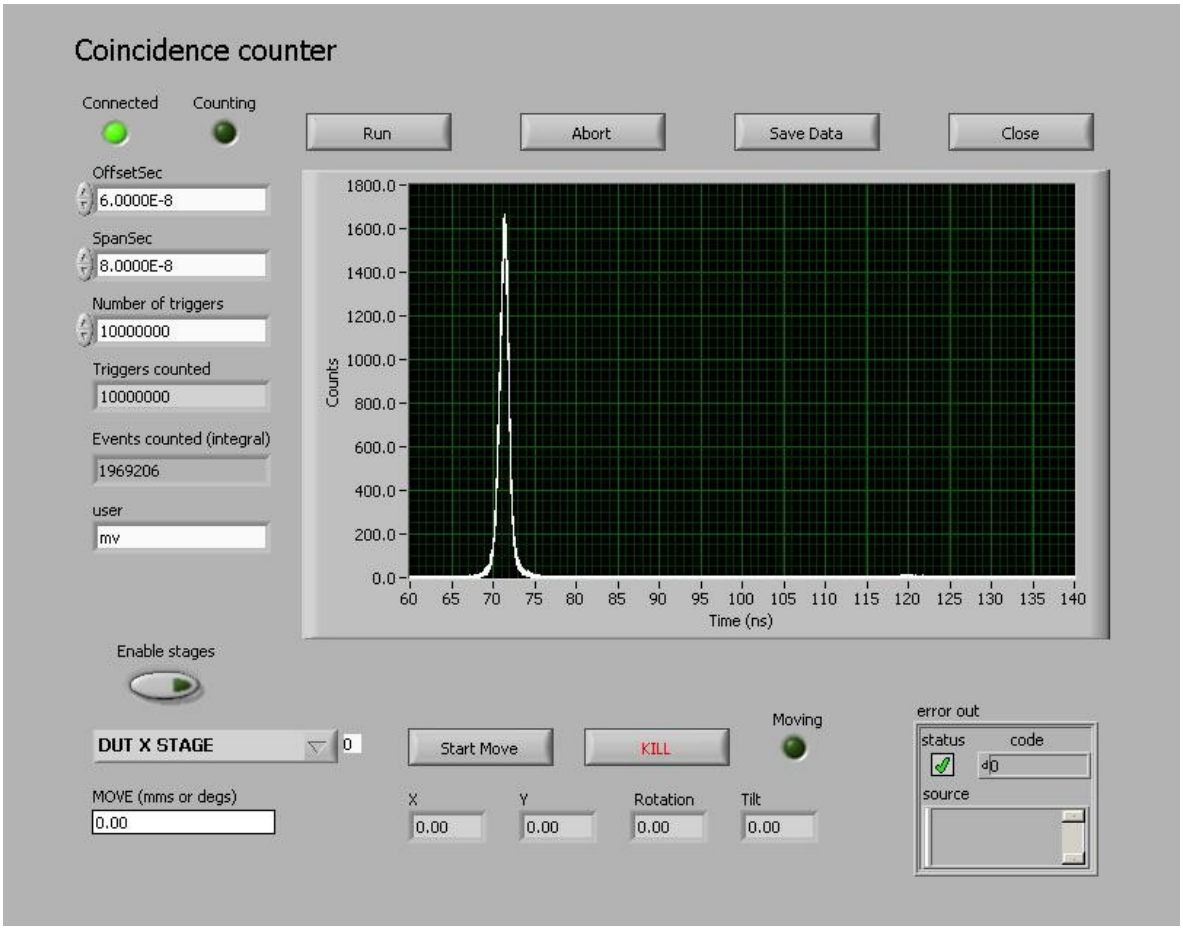

Figure C-3 *Coincidence counter (9308) window.*

The offset, span and number of triggers are set in the top left hand boxes. Whilst the counter is running, the 'Triggers counted' box and the graph are continually updated. At the end of the scan the 'Events counted' box is updated. This is the total number of events (from the DUT) counted during the scan. If necessary, the scan can be stopped by clicking on 'Abort'.

'Save data' saves the parameters, user, date and data from the histogram in a single column. Note that since the histogram has 65536 bins, the saved file will have too many rows to be opened directly in Excel. If this is required, the file must be opened in Notepad and the parameters removed.

If necessary, the stages can be moved to tweak the alignment. The ‘Enable stages’ button must toggled first to do so. Note that it is safer to leave this off if the alignment is fine to prevent accidental movement.

D. Photographs of the experimental set up for QE measurements

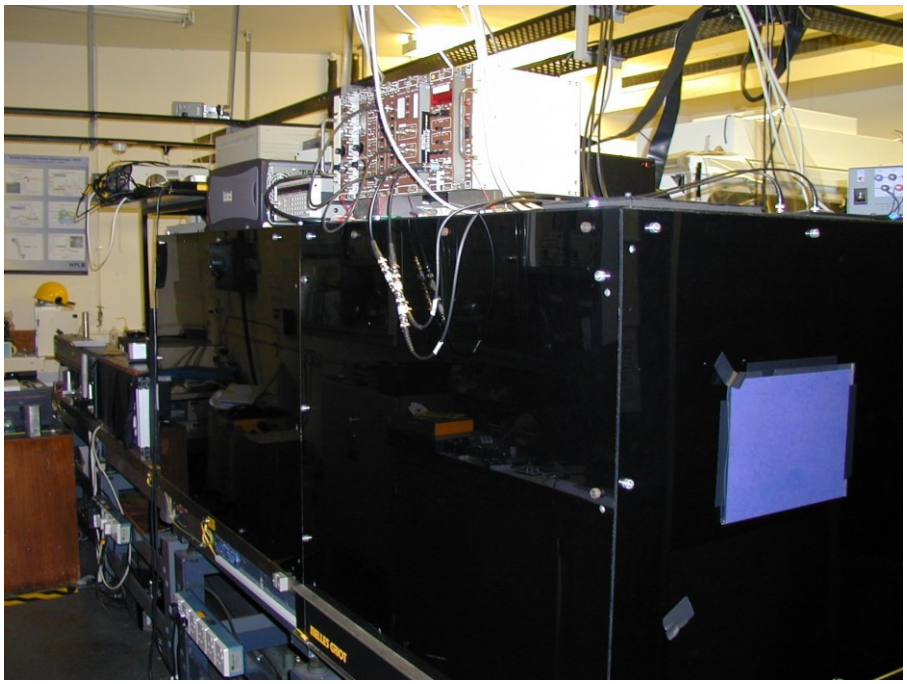

Figure D-1 *The light tight experimental enclosure. The argon laser can be seen in the background on the left. On top of the enclosure is the PC and counting electronics.*

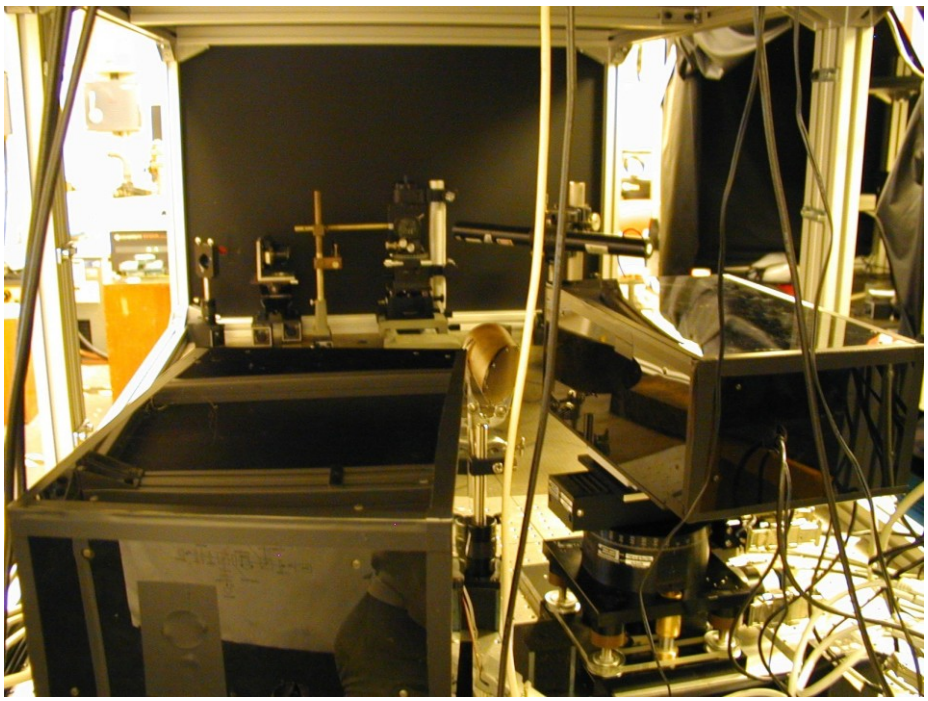

Figure D-2 *View from the end of the optical table with the side panels removed, looking from the detectors (in the boxes in the foreground) towards the crystal. The beam enters through a narrow band pass filter over an opening in the far panel.*

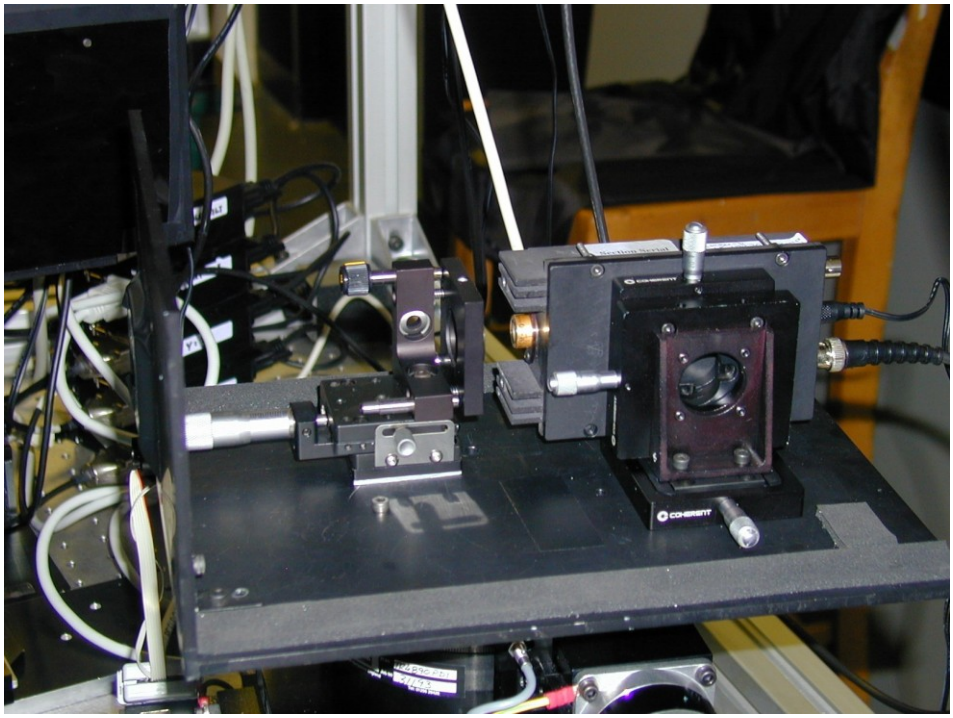

Figure D-3 *Detector assembly (trigger) with the light-tight cover removed. The filter is fixed to the front plate. The lens is mounted on the translation stage in the middle. On the right is the detector, mounted on x, y and z translation stages.*

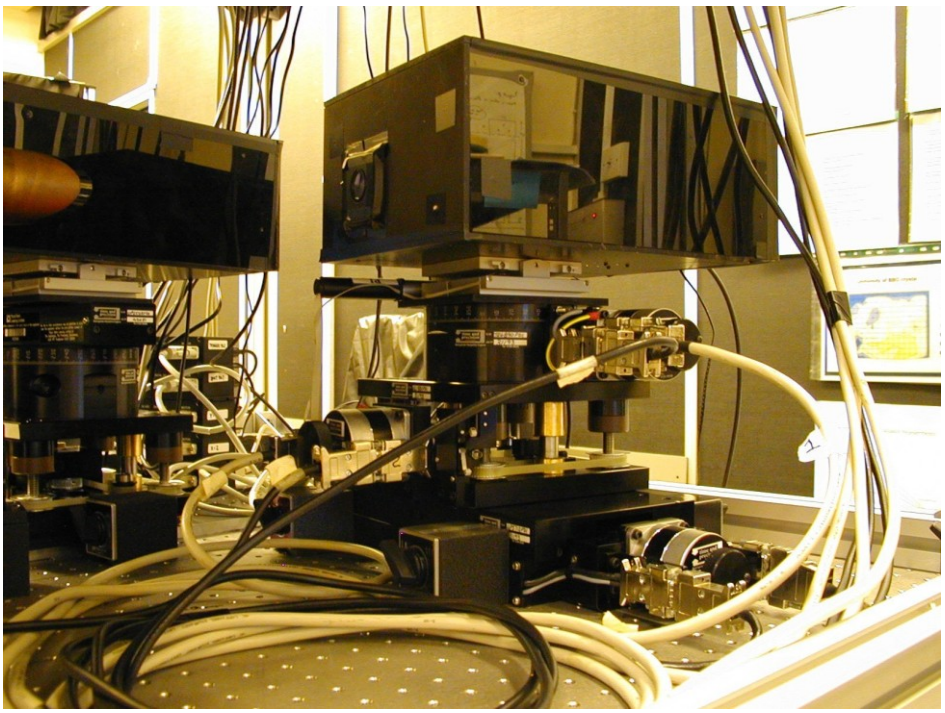

Figure D-4 *The trigger detector enclosed in its light tight box, shown mounted on the automated rotation and translation stages.*

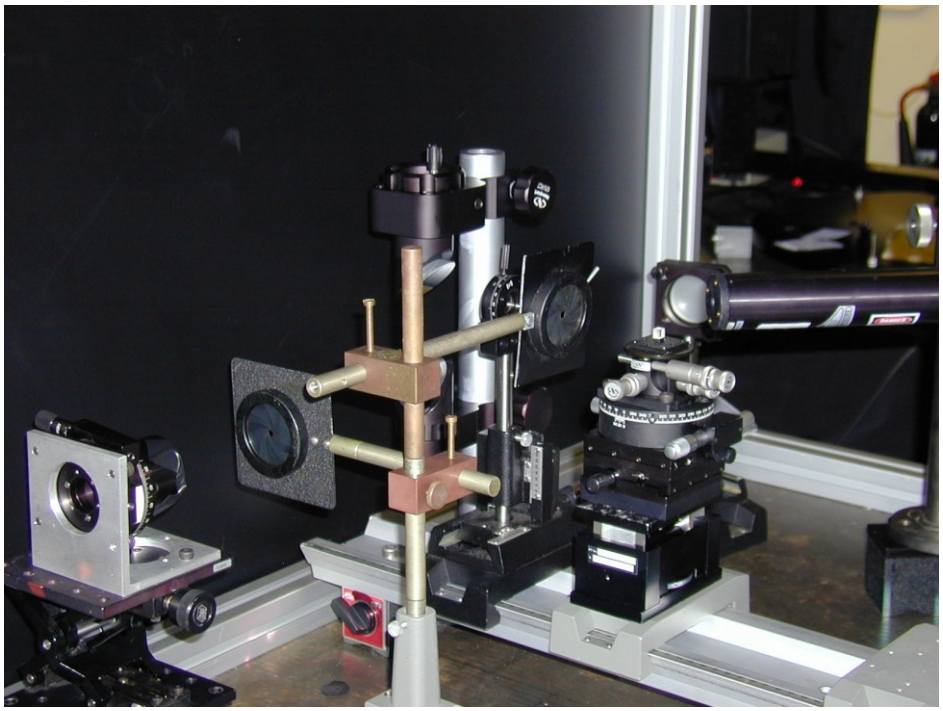

Figure D-5 *Mountings on the optical rail. On the left is the polariser (off rail). The HWP is somewhat obscured behind the iris mountings. Also obscured are the mirrors for reflecting the laser beam along the optical rail. The beam enters from the left. The crystal mounting is on the right. The HeNe laser just seen on the right hand edge is used for alignment.*

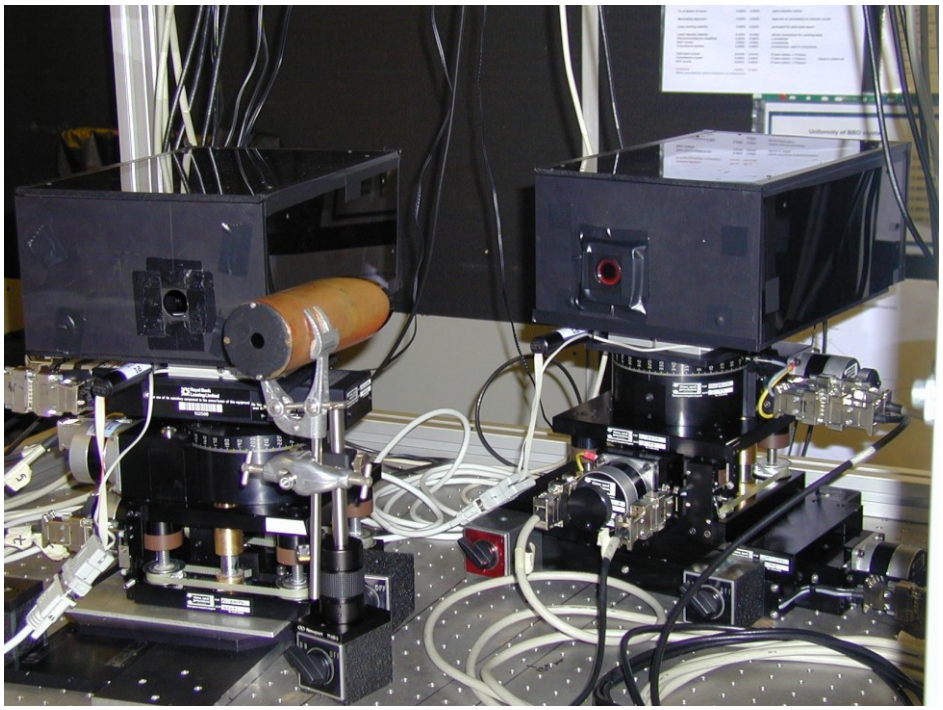

Figure D-5 *The detector stages seen from the front. The DUT is on the right and the trigger on the left. The filter has been removed from the DUT in the last round of measurements. The beam stop in the middle terminates the UV pump beam.*

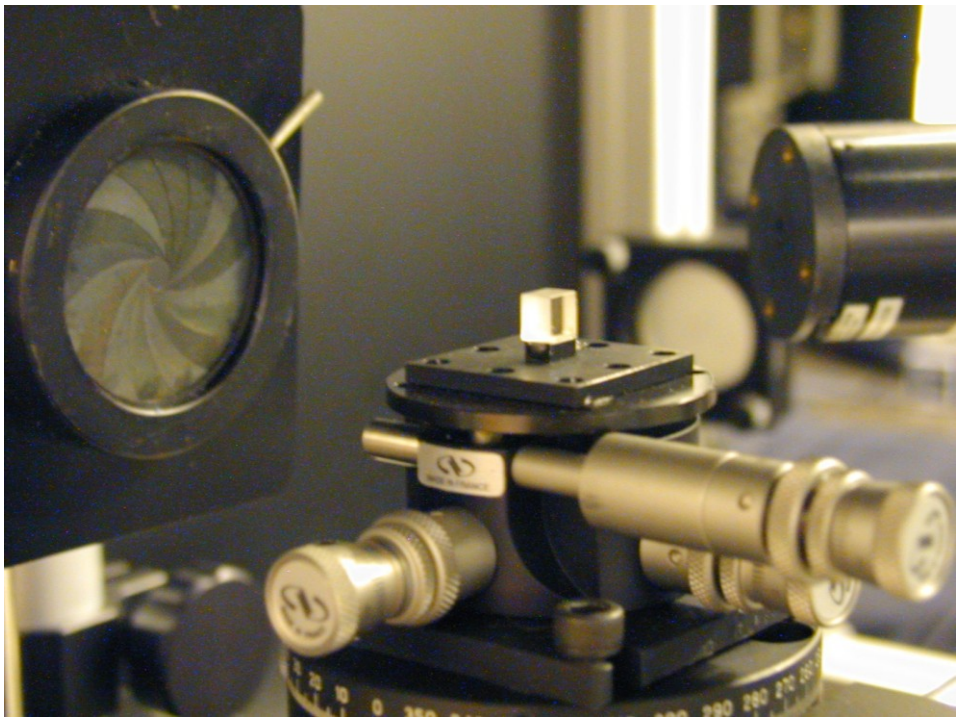

Figure D-6 *Close up of the BBO crystal used in the experiments. The crystal is mounted on rotation and tilt stages to enable adjustment for the normal incidence of the pump beam.*

E. SPCM-AQR series APDs.

Specifications for SPCM-AQ series. Data taken from **www.perkinelmer.com/opto**

Parameter	Minimum	Typical	Maximum	Units
Supply current		0.5	1.9	Amps
Supply voltage	4.75	5.0	5.25	V
PerkinElmer power cable total resistance		0.2		Ω
Case operating temperature	5		40	°C
Photon detection efficiency (Pd)@				
400 nm	2	5		%
650 nm	55	70		%
830 nm	40	50		%
1060 nm	1	2		%
Quantum Efficiency				
400 nm		2		%
650 nm		90		%
830 nm		92		%
1060 nm		18		%
Pd variation at constant casetemperature (2h @ 25° C)		± 1	±3	%
Pd variation 5° C to 40° C case temperature		± 4	±10	%
Dark Count				
SPCM-AQR-13		150	250	Counts/Second
SPCM-AQR-14		50	100	Counts/Second
Average dark count variation at constant case temperature (6 hrs @ 25° C) for (4,5,6);			± 10	%
SPCM-AQR-13			± 10	%
SPCM-AQR-14			± 1	σ

Parameter	Minimum	Typical	Maximum	Units
Average dark count variation at 5° C to 40° C case temperature for				
SPCM-AQR-13			± 20	%
SPCM-AQR-14			± 2	σ
Single Photon Timing Resolution		350		ps @ FWHM
Dead Time (Count rates below 5Mc/s)		50	~	ns
Output count rate before saturation	10	15		Mc/s
Linearity correction factor:				
@200 kc/s		1.01		
@1 Mc/s		1.08	1.15	
@5 Mc/s		1.40	1.67	
Afterpulsing probability		0.3		%
Settling time following power up (1% stability) @ 1 meg counts/sec and 25° C		15	30	S
Threshold setting required on counter for digital output pulse (terminate in 50 Ohms)	0.75	1.0	2.0	V
Pulse Width		30		ns
Gating turn on/off: (50 Ω output)				
Disable = TTL Low		2	4	ns
Enable = TTL High		45	55	ns
Gate Threshold Voltage:(@ V supply = 5V)				
Low level (sink current >90mA)		0	0.4	V
High level (sink current >30mA)		3.5	5.25	V

Detector pulse shapes (before attenuation and inversion).

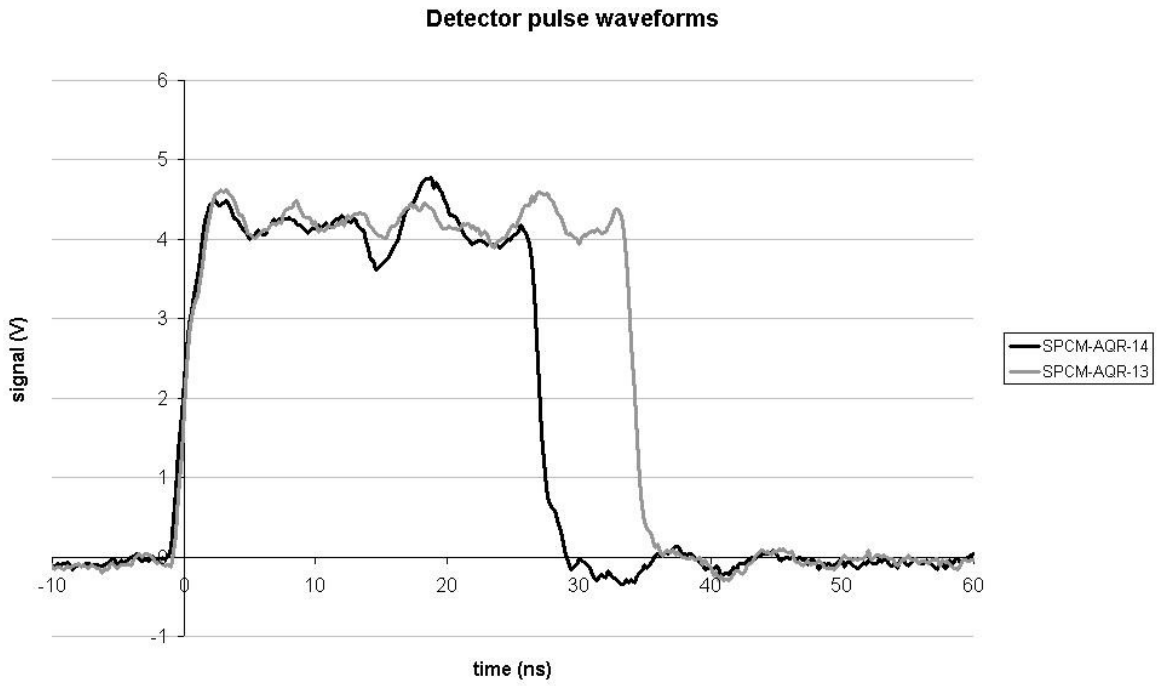

Figure C-1 *The waveforms of the APD detectors used. These graphs were obtained using an oscilloscope.*

8. References

[i] Aspect, A., Grangier, P., Roger, G., *Experimental Tests of Realistic Local Theories via Bell's Theorem,* Physical Review Letters, **47**, 460, (1981).

[ii] Fox, N. P., *Primary radiometric quantities and units*, Metrologia, **37**, 507-513 (2000).

[iii] Klyshko, D.N., *Utilization Of Vacuum Fluctuations as an Optical Brightness Standard.* Sov.J.Quant.Electron, **7**, 591-595 (1977).

[iv] Rarity, J. G., Ridley, K. D., Tapster, P. R., *Absolute Measurement of Detector Quantum Efficiency Using Parametric Downconversion*. Appl. Opt., **26**, 4616-4619, (1987).

[v] Migdall, A.L., Datla, R.U., Sergienko, A., Orszak, J.S., Shih, Y.H., *Absolute Detector Quantum-Efficiency Measurements Using Correlated Photons*, Metrologia, **32**, 479-483, (1995/96).

[vi] Migdall, A., Datla, R., Sergienko, A., Orszak, J.S., Shih, Y.H., *Measuring Absolute Spectral Radiance with Correlated Visible Photons: Technique Verification and Measurement Uncertainty*, Appl. Opt., **37**, 3455-3463 (1998)

[vii] Brida, G., Castelletto, S., Degiovanni, I. P., Novero, C., Rastello, M. L., *Quantum Efficiency and Dead Time of Single Photon Counting Photodiodes: A Comparison Between Two Measuring Techniques*, Metrologia, **37**, 625-628, (2000)

[viii] Migdall, A. L., Castelletto, S., Degiovanni, I. P., Rastello, M. L., *Intercomparison of a correlated-photon-based method to measure detector quantum efficiency*, Appl. Opt., **41,** (15), 2914-2922, (2002)

[ix] Dauler, E., Migdall, A.L., Boeuf, N., Datla, R.U., Muller, A., Sergienko, A.V., *Measuring absolute infrared spectral radiance with correlated photons: New arrangements for improved uncertainty and extended IR range*, Metrologia, **35**, 295-300, (1998)

[x] Butcher, P.N., Cotter, D. *The Elements of Nonlinear Optics*, Cambridge University Press (1990).

[xi] Louisell, W.H., Yariv, A., Siegman, A.G., *Quantum Fluctuations and Noise in Parametric Processes,* Phys. Rev, **124**, 1646-1654, (1961)

[xii] Kwiat, P.G., *Nonclassical Effects from Spontaneous Parametric Down-Conversion: Adventures in Quantum Wonderland*, PhD thesis, University of California at Berkley, (1993)

[xiii] Kleinman, D.A. Phys. Rev **, 126**, 1977-9 (1962).

[xiv] Dmitriev, V.G., Gurzadyan, G.G., Nikogosyan, D.N., *Handbook of Nonlinear Optical Crystals*, Springer Verlag, 2nd ed., (1997).

[xv] Eimerl et al., J. Appl. Phys., **62**, 1968 (1987)

[xvi] Migdall, A. L., *Correlated-photon metrology without absolute standards*, Physics Today, **52,** (1), 41-46 (1999)

[xvii] Cheung, J.Y., Vaughan, M.P., Mountford, J.R., Chunnilall, C.J., *Correlated Photon Metrology of Detectors and Sources*, Proc. SPIE (submitted 2003).

[xviii] Anderson, V.E., Fox, N.P., Nettleton, D.H., *Highly Stable Monochromatic And Tunable Optical Radiation Source And Its Application To High Accuray Spectrophotometry*, Appl. Opt., **31**, 536-545 (1992)

[xix] Hartree, W.S., Theocharous, E., Fox, N.P., *A Wavelength Tunable, Quasi-CW Laser Source for High Accuracy Spectrometric Measurement in the 200 nm to 500 nm Region*, Proc. SPIE, **4826**, 104-112 (2003)

[20] G. Ghosh, J. Appl. Phys., **78**, 6752 (1995).